Influence of recycled rubber mat on the behaviour of ballast under impact loading: Experimental and numerical modelling

Trung Ngo, PhD, MASCE

Senior lecturer, Transport Research Centre, School of Civil and Environmental Engineering, University of Technology Sydney, Ultimo, Australia.

Buddhima Indraratna, PhD (Alberta), FTSE, FIEAust, FASCE, FGS

Distinguished Professor of Civil Engineering and Director of Transport Research Centre, University of Technology Sydney, Ultimo, Australia; Founding Director, ARC Industrial Transformation Training Centre for Advanced Technologies in Rail Track Infrastructure (ITTC-Rail)

Matthew Coop, PhD

Professor of Geotechnics, Department of Civil, Environmental and Geomatic Engineering, Faculty of Engineering Science, University College London, UK

Yujie Qi, PhD

Lecturer, Transport Research Centre, School of Civil and Environmental Engineering, University of Technology Sydney, Ultimo, Australia.

Revised Technical Paper, Submitted to **Géotechnique**

Author for correspondence:

Distinguished Professor Buddhima Indraratna

Transport Research Centre

University of Technology Sydney

Ultimo, NSW 2007

Australia.

Ph: +61 2 9514 8000

Email: buddhima.indraratna@uts.edu.au

Influence of recycled rubber mat on the behaviour of ballast under impact loading: Experimental and numerical modelling

Authors: Trung Ngo, Buddhima Indraratna, Matthew Coop, and Yujie Qi

[a]Senior lecturer, Transport Research Centre, School of Civil and Environmental Engineering, University of Technology Sydney, Ultimo, Australia; Email: Trung.Ngo@uts.edu.au

[b]Distinguished Professor of Civil Engineering and Director of Transport Research Centre, University of Technology Sydney, Ultimo, Australia; Founding Director, ARC Industrial Transformation Training Centre for Advanced Technologies in Rail Track Infrastructure (ITTC-Rail). Email: buddhima.indraratna@uts.edu.au

[c]Professor of Geotechnics, Department of Civil, Environmental and Geomatic Engineering, Faculty of Engineering Science, University College London, UK. Email: m.coop@ucl.ac.uk

[d]Lecturer, Transport Research Centre, School of Civil and Environmental Engineering, University of Technology Sydney, Ultimo, Australia; Email: Yujie.Qi@uts.edu.au

Abstract:

During the passage of trains, dynamic impact loads caused by wheel imperfections or rail abnormalities cause significant ballast degradation. In this study, the use of rubber mats manufactured from recycled tyres placed underneath a ballast layer is investigated to mitigate the adverse effects of impact loads. Based on a series of tests conducted using a high-capacity drop-weight facility to evaluate the dynamic impact responses, the experimental results show that the inclusion of a rubber mat beneath the ballast assembly significantly reduces particle breakage. This study also describes a numerical analysis following a coupled discrete-continuum modelling approach to examine the complex interaction of discrete ballast grains with the recycled rubber mat. In particular, a mathematical framework coupling the discrete and continuum domains is developed to facilitate the exchange of forces and displacements at the ballast-mat interface. Laboratory data measured from large-scale impact tests are used to calibrate and validate this coupled model. Subsequently, the model is used to predict the deformation and breakage of ballast, contact force distributions, impact forces, coordination numbers and the evolution of energy components during impact testing. The energy-absorbing properties of the rubber mat are captured in terms of reducing particle breakage from a micro-mechanical perspective.

Keywords: Ballast, Impact loading, Rubber mat, Numerical modelling, Particle breakage

INTRODUCTION

Railways are the most in-demand and widely used mode of transport in Australia, having a network of almost 40,000 kilometres of tracks. Rail tracks are usually built on a coarse granular medium known as ballast because (i) it is abundant and available, (ii) it has rapid drainage, and (iii), it has a high load-bearing capacity (Selig and Waters 1994, Indraratna *et al.* 2013). However, the increased axle loads of heavier freight trains and faster passenger services cause the ballast to deteriorate, with a consequent loss of track geometry and more frequent maintenance (Esveld 2014, Indraratna and Ngo 2018). More severe deformation often occurs when tracks are subjected to high impact loads caused by abnormalities such as crossings and turnout, and wheel/rail imperfections such as wheel defects and dips in the rails. Moreover, repeated train loading degrades and fouls the ballast aggregates, which leads to increased settlement, decreased shear strength, and reduced porosity that impedes the drainage capacity of the ballast layer (Tutumluer *et al.* 2013, Le Pen *et al.* 2016, Ramos *et al.* 2002). Previous studies have shown that subjected to repeated train loading, the shear strength, angularity and surface roughness of ballast reduced due to ballast fouling and breakage (Sun *et al.* 2019, Wong and Coop 2020). As a consequence, the degradation of ballast seriously hampers the safety and efficiency of rail tracks, and often leads to enforced speed restrictions and more frequent track upgrading (Suiker and Borst 2003, Priest *et al.* 2010). In practice, degraded ballast assemblies must be replaced with fresh ballast through frequent track maintenance. In the absence of quantified design specifications and guidelines that incorporate the adverse effects of particle breakage, the Australian rail industry spends hundreds of millions of dollars annually on track maintenance and the replacement of degraded ballast.

Discovering ways to improve the performance of ballast, minimise its degradation, and control track settlement is a significant challenge in railway practice. Previous studies show that planar polymeric geogrids (Bathurst and Raymond 1987, Raymond and Ismail 2003, Brown *et al.* 2007) and cellular inclusions (e.g., geocells) could improve track stability (Leshchinsky and Ling 2013, Biabani *et al.* 2016). Moreover, the ability of geogrid reinforcement to provide lateral and vertical constraints to ballast has been emphasised (Giroud and Han 2004, Konietzky *et al.* 2004, Shukla and Yin 2006). However, traditional plastic geogrids placed beneath the ballast layer do not provide enough damping or absorb the energy transferred to the track substructure by impact loads (Chen *et al.* 2013, Indraratna *et al.* 2019). For instance, over stiff foundations such as concrete bridge decks, rock subgrade or level crossings, traditional geogrids do not mitigate ballast breakage.

In the recent past, rubber mats have been trialled to reduce the deformation and degradation of ballast aggregates while enhancing overall track stability (Auersch 2006, Anastasopoulos *et al.* 2009, Alves

Costa *et al.* 2012). In fact, placing rubber inclusions such as under-sleeper mats and under-ballast mats has proven to be an effective method for attenuating the stresses transferred to the track substructure under monotonic and cyclic loadings (Le Pen *et al.* 2018, Sol-Sánchez *et al.* 2020, Moubeké *et al.* 2021). Laboratory test results have indicated that placing a layer of rubber inclusion in track substructure could reduce the amount of ballast breakage (Navaratnarajah *et al.* 2018, Xin *et al.* 2020, Moubeké *et al.* 2021). Other forms of rubber including rubber crumb, waste tyres, gravel/rubber mixtures have also been used for road and rail projects worldwide. A comprehensive study on the benefits of using recycled rubber mats to reduce ballast breakage will greatly benefit rail industry in future design and maintenance, given the rail industry push to embrace a circular economy perspective.

Railway noise and vibrations (particularly in urban areas) have been considered as one of the most challenging railway engineering practices in recent decades (Müller 2008; Sadeghi and Esmaeili 2017). There have been numerous studies on noise and vibration mitigation for rail system through field investigation, analytical and numerical modelling approaches (Anastasopoulos et al. 2009, Connolly et al. 2014). Under ballast mats have been used in rail tracks for mitigating noise and rail vibrations. They also serve as an effective vibration isolation layer, reducing the transfer of mechanical energy from passing trains into the track substructure, thereby decreasing both ground-borne vibrations and noise levels (Hanson and Singleton 2006, Sadeghi et al. 2019).

Lim *et al.* (2020) carried out DEM-FEM simulations of drop tests, investigating the interaction of ballast and train wheels. In this study, ballast aggregates were modelled as rigid spheres and therefore the breakage and angularity of particles could not be captured. Ngo and Indraratna (2020) studied the role of under-sleeper pads in attenuating the load applied in ballast assembly by mean of laboratory tests and DEM simulation. Although ballast breakage was captured in the study, the DEM analysis was carried out in 2D and the angularity of ballast particle was not accurately simulated. Jia *et al.* (2023) perfomed 2D and 3D DEM simulations to investigate the effect of a new sleeper with wedge-shaped geometries has on contact forces and sleeper displacement. However, ballast breakage and layered track substructure (capping, subgrade) were not considered.

In this study, a 10 mm thick rubber mat manufactured from scrap tyres is placed underneath a ballast layer. In essence, such a mat is expected to serve as a rubber energy absorbing layer (REAL) within the track substructure, hence less of the kinetic energy from the moving trains is transferred to the ballast layer, thus resulting in decreased particle breakage. The recycled rubber mat (REAL) used in this study can be categorised as elastomers consisting of a mixture of rubber particles (obtained from the shredding of waste tyres) and resin, which acts as a matrix binding rubber particles together (Sol-Sánchez *et al*. 2015, Mondragon-Enguidanos *et al*. 2021). A series of large-scale impact tests were carried out using a high-capacity drop-weight facility. The laboratory data complements the numerical analysis based on a coupled discrete-continuum modelling approach (i.e., coupled DEM-FDM) that quantifies the role of REAL in reducing the deformation and degradation of ballast aggregates from a micromechanical perspective.

The novelty of this study is to investigate the effect of recycled rubber mats on the deformation and degradation of ballast, employing both laboratory and discrete element modelling. To the knowledge of the authors, no previous attention has been given to: (i) how impact loads produced by heavy haul trains can be alleviated by rubber inclusions in a track substructure, and (ii) evaluating and quantifying the complex degradation and/or settlement of ballast subjected to impact loading. The current DEM analysis does provide a deeper insight into how the role of a recycled-rubber energy absorbing layer (REAL) influences particle breakage and plays an important part in the distribution of contact forces, particle displacement vectors, and coordination number (C_n). Obviously, none of these aspects could be captured through experimental data in the laboratory environment. In this regard, both experimental and DEM observations are imperative for a better understanding of how the REAL placed underneath the ballast layer effectively attenuates impact forces and influences the contact force transmission and the associated ballast breakage in a quantified manner.

In addition, the laboratory efforts demonstrated that the presence of REAL decreased ballast breakage. In support of this, the DEM analysis was able to convincingly explain that REAL partially absorbs impact forces across the granular mass, thus resulting in decreased particle-particle contact forces as well as the associated breakage of particles. The link between the experimental and numerical (DEM) phases is thereby established. The outcome of this study could facilitate the future design and establish the much needed practice guides for railway practitioners. To further demonstrate these benefits, a field trial conducted in Singleton, NSW showed that placing these rubber energy-absorbing mats on very stiff subgrade or concrete bridge decks could generate substantial savings up to several millions of dollars annually, by reducing the traditional ballast thickness from 300mm to 250mm, and more effectively controlling the particle breakage (Indraratna *et al.* 2014). In addition, the savings generated by the reduced need for quarrying fresh aggregates have a direct environmental benefit through curtailing the excessive degradation of rocky landscapes.

LABORATORY TESTING PROGRAM

High-capacity drop-weight impact testing facility

High-capacity drop hammer impact testing equipment is used to study the effect that REAL has on the attenuation of dynamic impact loads and the subsequent reduction in ballast breakage (Fig. 1a). This impact apparatus consists of a free-fall hammer (590 kg) that can be dropped from a specified height onto the ballast sample, h_d =100-250 (mm). It is noteworthy that this equipment is cylindrical and therefore, due to the size and shape of the test specimen (300 mm diameter, 560 mm height), a real-life sleeper could not be included. Instead, a steel cylindrical plate (50 mm thick) was used to transfer the impact load at the top surface of the ballast layer. To determine stresses, preliminary tests were carried out in the laboratory with a rigid steel pressure plate (200 mm diameter, capacity 1MPa) placed on the top surface of the ballast layer subjected to varying drop heights (h_d). In this regard, this type of impact testing may not be perfectly representative of the physical sleeper-ballast assembly in the field, where the stress propagated to the underlying substructure is based on axial load spreading over a set of adjoining sleepers using a trapezoidal distribution. However, the current method is altered for laboratory simulation where the vertical stress at the ballast-sleeper interface upon impact loading can still be mimicked accurately. The range of drop height and the drop mass are specifically selected to produce a vertical stress on the ballast surface in the range of σ_I=300-600 kPa that is representative of typical impact stresses generated by corrugated rails, wheel flats or dipped rail joints based on field measurements (Remennikov and Kaewunruen 2014, Indraratna et al. 2010). A 10 mm thick layer of REAL made from waste tyres is placed under the ballast layer (Fig. 1b). Details of the instruments, placement of track substructure layers, as well as a plan view and cross-section of the impact testing facility are shown in Figure 1.

An accelerometer (Isotron, model 41A, capacity of up to 500 g) was mounted on the top of the loading plate (Fig. 1b), measuring the acceleration of the ballast assembly. Epoxy resin was used to connect the accelerometer onto the steel plate and it was carefully checked after every hammer drop to ensure the device functioned properly. The data logger acquisition system (DT800) was controlled by a host computer supported by LabVIEW software to accurately record impact forces, vertical displacements and accelerations at predetermined time intervals during the testing phase. To reduce signal noise, the raw impact load-time histories were digitally filtered using a low-pass fourth-order Butterworth filter with a sample rate of 2,000 Hz. A dynamic load cell, with a capacity of 1,200 kN was attached to the drop hammer and it was connected to a host computer-controlled data acquisition system to measure the impact forces during testing.

Sample preparation and materials used in the test

Crushed basalt consisting of igneous rock aggregates (latite basalt) collected from Bombo quarry (New South Wales, Australia) and which comply to Australian standard gradation (AS 2758.7: 2015), is used in the laboratory (Figs. 2a-2b). The ballast was sieved, washed, mixed and then placed inside a cylindrical rubber membrane in three separate layers and compacted to a density of 1560 kg/m^3 (initial void ratio, e_o=0.74, specific gravity, G_s=2.7), simulating a typical field density attained by vibratory tamping in most Australian heavy haul tracks. The ballast specimen was assembled using a 7 mm thick cylindrical rubber membrane with a 300 mm diameter to prevent piercing by sharp particles during testing (Fig. 1c). During the compaction, the sample was supported by two halves of a steel mould that surrounded the cell membrane. It is noted the applied radial pressure from the membrane to the ballast specimen is expected to vary with the lateral displacements. After compacting the ballast layer in the assembly, a 50mm steel plate (loading plate) was fitted at the top of the ballast and fastened by steel ties. The capping material (sub-ballast) is a mixture of sand and crushed rock (Fig. 2c) that is placed under the ballast layer (d_{max} = 19 mm, d_{min} = 0.075 mm, d_{50} = 2.9mm) and compacted to a unit weight γ_d = 20.5 kN/m^3 and a thickness of 100 mm. A mixture of sandy-clay soil (50mm-thick) is placed underneath the capping layer and compacted to a bulk unit weight of 18.5 kN/m^3 (at 7% moisture content) to simulate a soft subgrade. The particle size distributions of the materials used in these laboratory tests are shown in Figure 3. A layer of recycled rubber mats (Fig. 2d) is used as a REAL layer to be placed underneath the ballast layer. The thickness of the rubber mat (REAL) and its mechanical properties (i.e., static/dynamic bedding modulus) will affect its performance. In this study, the rubber mats (10 mm thick) were produced locally from recycled tyres, which is one of the most common thicknesses to be used as shock absorb mats in rail tracks (Nimbalkar et al. 2012, Navaratnarajah and Indraratna 2017). Also, this selection of 10mm was partly influenced by a manufacturing process. In addition, 10 mm thickness rubber mats have been tested previously for a real freight track in the town of Singleton, NSW, Australia (Indraratna *et al*. 2014), and subsequently adopted by Australian heavy-haul rail organisations. It is noted that there are other commercially available rubber mats with thickness varying from 7mm to 44 mm (Sol-Sánchez *et al*. 2014). The 10 mm thick rubber mat used in the study was made from 1-3 mm size recycled rubber granulates bound by a polyurethane elastomer compound. The mechanical properties of the rubber mats (REAL) and both static and dynamic properties have been evaluated as per established testing standards stipulated in DIN 45673-5 (DIN 2010). Three squared samples (200 mm × 200 mm) were used for the measurement of dynamic properties of REAL. The bedding modulus is calculated in Equation (1), as the secant modulus from the average results from the three tests. Based on these test results, the value of static bedding modulus, C_{stat} is 0.142 N/mm^3 while the dynamic bedding modulus, C_{dyn} varies from 0.107 N/mm^3 to 0.148 N/mm^3 over the frequency range of f = 5-30 Hz. The mechanical properties of REAL used in the laboratory are summarised in Table 1. Sol-Sánchez et al. (2014) carried out tests on different types of ballast mats made from destructed tyres with thicknesses between 11.0 and 44.0 mm and reported that the values of static C_{stat} =0.1–0.73 N/mm^3 while the dynamic C_{dyn} = 0.113–1.65 N/mm^3 at f=5–10 Hz. Recently, Esmaeili *et al*. (2023) carried out environmental tests to evaluate the applicability of using recycled plastics in making railway sleepers and they found that the electrical resistance of the recycled plastic material was almost 1.5 times the corresponding value of concrete sleepers, and they could be considered as a suitable alternative for sleepers made from recycled plastics in rail tracks.

$$C_{stat/dyn} = \frac{\Delta F}{A_0 \times \delta h} = \frac{F_2 - F_1}{A_0 \times \delta h} \quad (\text{N/mm}^3) \tag{1}$$

where, A_0 is the plan area of REAL (mm^2); F_2, F_1 are the maximum and minimum applied cyclic load; and δh is the compression of REAL during loading/unloading (mm).

A series of tests took place with and without the inclusion of REAL under varying drop heights of h_d = 100 mm to 250 mm and these test data are adopted in this study to compare with the numerical analysis. In summary, the results show that the inclusion of REAL could reduce the deformation and breakage of ballast subjected to impact loads. The impact loads varied from 50 to 750 kN over a duration of about 10 ms, during which time REAL significantly attenuated the magnitude of the impact loads. The test data also indicated that the beneficial effects of REAL are better when it is placed on a concrete panel (i.e., simulating a bridge deck), where ballast deformation decreased by about 15% and ballast breakage by about 17%.

DISCRETE ELEMENT MODELLING FOR IMPACT TESTS

The discrete element method (DEM) first introduced by Cundall and Strack (1979) has been widely used to study the micro-mechanical behaviour of granular materials (Jiang *et al.* 2005, McDowell *et al.* 2006, O'Sullivan and Cui 2009, among others). DEM can examine various aspects of particle breakage (Lobo-Guerrero and Vallejo 2005) such as the influence of irregularly shaped grains, the evolution of contact force distributions (Guo *et al.* 2020), and the linkage between macro and micro properties (i.e., anisotropy, fabric, coordination numbers) that are often challenging to obtain via continuum modelling (Lim and McDowell 2005, Bolton *et al.* 2008, Huang and Tutumluer 2011). In this study, DEM is used to understand and quantify the load-deformation response of ballast subjected to impact loading after incorporating REAL in the track substructure.

The process of parameterizing the DEM model is acknowledged to be complex due to its strong reliance on factors such as the representation of particle shapes, the particle-particle contact law, and the loading conditions being simulated, such as static or impact loads. Suhr *et al.* (2022) introduced an advanced contact law, Conical Damage Model (CDM) to model railway ballast, considering additional physical effects (e.g. edge breakage) occurring in the experiment. A parametrisation strategy was proposed to calibrate different DEM models and to study the influence of particle shape. Recently, Jia *et al.* (2023) investigated the influence of particle shape, contact properties on the force behaviour of ballast in DEM and introduced a method to improve the efficiency of DEM calculations. An optimised multi-layer DEM model was formulated, where the ballast in the most influential area is simulated by the irregular elements with a linear contact model, and other particles are the ball elements with rolling resistance. This modelling approach allows to reduce the number of elements to the largest extent and thereby, reduces calculation time.

It is noted that the imaging technique has been adopted by others to simulate the angular shape and breakage of granular materials (Tutumluer *et al.* 2012, Zhao *et al.* 2015, Wu *et al.* 2023, among others). In this study, a total of 10 representative particles of ballast were taken from the laboratory (Fig. 4a) and scanned by a 3D laser scanner (VIVID 910) to simulate the geometry of these irregularly shaped particles. Polygonal meshes of these particles were digitised to simulate their angularity and shape, as shown in Fig. 5a. Appropriate subroutines were developed (FISH language) to build ballast particles in DEM by bonding a number of spheres together and filling up the polygonal mesh. The linear parallel-bond contact model was developed by Potyondy and Cundall (2004) and it has been widely used to model a range of geomaterials including, ballast, sand, aggregates and geosynthetic materials (Wang and Leung 2008, Jo *et al.* 2011, Li *et al.* 2020). The bond strength is defined by multiple input parameters, including the normal and shear bond stiffness, denoted as k_{pn} and k_{ps}, respectively, and bond strength (s_p) which are the main control parameters of the parallel bond model (Table 2). The parallel-bond interface is distributed over a circular cross-section lying on the contact plane and centred at the contact point. It can transmit both forces and moments, which means it can resist relative rotation until the imposed load exceeds its limiting strength. The breaking of bonds within a simulated particle is considered to represent ballast breakage. As stated by Cundall (2001), a calibration process is needed for acquiring all input micro-parameters, which commonly involves a trial-and-error process. In this study, the calibration of the bond strengths for ballast particles was carried out using a compression test (Fig. 4b). The parallel bond strength was determined based on matching the load-displacement responses that were obtained from laboratory compressive tests with those predicted from DEM. Ballast particles are generated inside the impact test apparatus following the particle size distribution

(AS 2758.7-2015) at random orientations in order to resemble the experimental conditions. The void ratio of the simulated ballast assembly is 0.74, which is similar to the ballast samples tested in the laboratory.

Coupled discrete-continuum analysis

The continuum modelling approach can handle large-strain deformation within a reasonable computational time, but it cannot account for the effect of particle angularity and breakage (Breugnot *et al.* 2016, Song *et al.* 2019). Hence, there is an imperative need to introduce a coupled discrete-continuum approach (i.e., coupled DEM-FDM) that utilises the advantages of both numerical methods. In this study, the surrounding rubber membrane is simulated by the continuum approach using an elastic constitutive model where the membrane consists of edge-connected, triangular faces where the vertex velocities and positions are specified using a shape function (Fig. 5b). This coupling logic takes the contact forces with wall facets and determines an equivalent force system at the vertices of the facets; these forces are then distributed to the nodes with the corresponding stiffness contributions. The rubber energy absorbing layer (REAL), and the capping and subgrade layers are simulated as continuum elements (Fig. 5c). The drop hammer consists of a rigid body with a mass of 590 kg being dropped from varying heights of h_d =100 mm to 250 mm (Fig. 5d).

Determination of input parameters for the coupled DEM-FDM

The micro-mechanical input parameters used to simulate the ballast in DEM are derived by calibrating the shear-stress strain responses with laboratory tests carried out earlier by the authors (Indraratna *et al.* 2011). The parameters are then varied interactively until the predicted shear stress-strain responses corroborate with those measured experimentally. The bond strength of ballast is selected by conducting triaxial tests on cylindrical rock samples. During a triaxial test, the sample is confined and then sheared until failure, which allows for the determination of its shear strength properties. The DEM model carried out in this study is a fully dynamic formulation, thereby damping is necessary to dissipate kinetic energy. It is noted that there are several parameters contributing to the dynamic behaviour of the materials. Damping is essential for dissipating kinetic energy and controlling vibrations where the damping factor (loss factor) is a key parameter for understanding how a material dissipates energy (ability to absorb and dissipate energy) when subjected to dynamic loading. Stiffness quantifies the material's resistance to deformation under dynamic conditions. Also, the thickness and contact area are also significant factors that influence how stresses and strains are distributed within the material. These concepts have been captured in the current coupled discrete-continuum analysis.

The drop of the 590 kg hammer generates a substantial dynamic impact, and therefore, a high value of damping coefficient (ζ) is required for energy dissipation. Trial simulations have been conducted at smaller values of ζ varying from 0.0 to 0.6, however, the numerical model did not converge to a stable condition when subjected to high impact forces. There is a correlation between model convergence and damping values in simulations, particularly for dynamic analyses subjected to high-impact loading. If damping values are too low (under-damping), the oscillations caused by dynamic loading can prevent the simulation from reaching a stable state, i.e., leading to very gradual convergence. In contrast, high damping values are often used for dissipating energy and preventing the system from experiencing unrealistic oscillations (resonance). In this regard, high damping values are often used for suppression of the resonance region rather than attenuating the load amplitude, and the current DEM analysis does not contradict this. In this study, the energy dissipation is achieved by the way of interparticle friction and global damping used in tandem. The friction coefficient for ballast can be simulated approximately by μ = 0.85 (Indraratna *et al*. 2011) and a damping coefficient of ζ = 0.7 is adopted to to prevent the system from entering a resonance region that can induce large oscillations leading to excessively large deformation. It is noted that the damping coefficient of ζ = 0.7 has been commonly adopted by researchers in the past to simulate ballast in DEM (Li and McDowell 2020; Jia *et al*. 2023, among others).

REAL is modelled as a linear elastic material having an elastic modulus of E=15.68 MPa, as determined from static compression tests. To increase numerical stability, a value of damping ratio for the REAL of 0.114 was used in the current analysis. It is noted that the stiffness and other property parameters (e.g., density, Elastic modulus E, Poison's ratio ν, cohesion c, friction angle ϕ, and dilatancy angle ψ) of the capping and subgrade layers influence the research results and higher impact forces are found to develop for a stiffer subgrade (Nimbalkar *et al*. 2012). For instance, stiffened substructures consisting of concrete decks (bridges and tunnels) or rock foundations can generate high-impact loading contributing to track component failures and increased maintenance costs (Chumyen *et al.* 2022, Shan *et al.* 2020). In this study, the tested capping and ballast materials were selected to represent typical track substructure conditions in Bulli and Singleton, NSW, Australia, as carried out earlier by Indraratna *et al.* (2010, 2014). The track was built over a stiff subgrade consisting of over-consolidated silty clay (estuarine) intermixed with shale cobbles and gravels with adequate strength to sustain heavy haul trains. The material parameters were determined from laboratory testing conducted on the capping and subgrade materials, including oedometer test, large-scale direct shear tests and triaxial tests. The density of capping and subgrade was selected as 1,955 kg/m^3 and 1,850 kg/m^3 which are similar to those carried out in the impact tests. Based on oedometer tests, the elastic modulus of capping and subgrade was determined as 120 (MPa) and 55 (MPa), respectively. It is noted that the capping layer was highly compacted to provide an impervious layer that laterally diverted infiltrated rainwater to the side drain and drainage to decrease the load propagating to the soft subgrade soft clay. A small value of cohesion (2 kPa) for capping was utilised to enhance the numerical stability. Friction angles of capping and subgrade were determined as ϕ=39^0 and 25^0, respectively from direct shear tests while the dilation angle, ψ =9^0 was determined from triaxial tests. Given the main objective of this study is studying the role of recycled rubber mat on the behaviour of ballast under impact loading, the capping and subgrade (assumed fully drained) are modelled using an elastic-fully plastic model that embraces the Mohr-Coulomb yield criterion. The relevant material properties adopted in the numerical analysis are summarised in Table 3. Once a simulated impact test is set up, the model is then run to bring it into initial equilibrium, facilitating the particles to form contact with each other, while the unbalanced forces remain almost unchanged at about 12.5×10^{-2} N. The simulated hammer is then raised to a height of h_d = 100, 150, 200 and 250 mm and then released to drop onto the ballast assembly. During the simulated drop heights, the impact forces, vertical settlement, and lateral displacements are recorded, and micromechanical properties such as the contact forces, coordination numbers, number of broken bonds, and evolution of energy components are captured and analysed to investigate how REAL helps to reduce the deformation and breakage of ballast.

Implementation of force-displacement exchanges for coupled discrete-continuum modelling

An exchange of force-displacement between the discrete ballast particles and continuum elements must be established to perform a numerical analysis (Fig. 6). When subjected to impact loads, contact forces develop across the ballast aggregates; these contact forces act as enforced boundary conditions to the relevant finite element mesh. A mathematical framework for the coupling scheme between a discrete particle and continuum element (O'Sullivan 2011, Itasca 2020) is formulated below:

Contact forces in the DEM domain are computed as: $F_i^{[C]} = F_n^{[C]} + F_s^{[C]}$ (2)

In the above, the normal contact force ($F_n^{[C]}$) is calculated as: $F_n^{[C]} = K^n U^n n_i$ (3)

and the contact shear force is determined in an incremental form as:

$$\Delta F_s^{[C]} = -K^s \left(\Delta X_i^{[C]} - \Delta X_i^{[C]} n_i\right) \quad (4)$$

Resultant forces and moment acting on particles are calculated as:

$$F_i^{[P]} \leftarrow F_i^{[P]} - F_i^{[C]}, \text{ and } M_i^{[P]} \leftarrow M_i^{[P]} - e_{ijk}\left(X_j^{[C]} - X_j^{[P]}\right) F_k^{[C]} \quad (5)$$

The relative velocity (V_i) at the interface is determined by (Itasca 2020):

$$V_i = \dot{X}_{i,E}^{[C]} - \dot{X}_{i,E}^{[P]} = \dot{X}_{i,E}^{C} - \left[\dot{X}_i^{[P]} + e_{ijk}\omega_j^{[P]}(X_k^{[C]} - X_k^{[P]})\right] \quad (6)$$

where, $\dot{X}_{i,E}^{[C]}$and $\dot{X}_{i,E}^{[P]}$ are the velocities of a continuum elements and discrete particles, respectively. $\dot{X}_i^{[P]}$and $\omega_j^{[P]}$ are the translational and rotational of the particles, and $e_{ijk}$is the permutation symbol.

The velocity (displacement) of continuum elements at the interface is computed as:

$$\dot{X}_{i,E}^{[C]} = \sum N_j \dot{X}_{i,E}^{j} \quad (7)$$

where, $N_j$is a shape function given by: $N_j = (1 + \xi_o)(1 + \eta_o)/4, j = 1,2,3,4$; and $\xi_o = \xi_i\xi, \eta_o = \eta_i\eta$; $\xi_i$and $\eta_i$are local coordinates of nodes.

At the interface, the shear and the normal contact forces (Appendix A) are distributed to the nodal force, $F_i^{[E,j]}$ follows the shape function N_j as given by:

$$F_i^{[E,j]} = F_i^{[E]} + F_i^{[C]} N_j \quad (8)$$

At a given time Δt, the contact forces in the DEM domain transfer to the continuum zone as boundary forces. The nodal displacements in the continuum zone are then transferred back to ballast particles as boundary displacements, thus executing a fully coupled simulation, as detailed in Appendix A. The coupled model is then validated by comparison with the prototype test data obtained earlier by Ngo *et al.* (2019).

Theoretical Considerations: Energy absorbing capacity of REAL

It is assumed that at a given drop height (h_d) the impact energy provided by the dropping hammer is transferred to various energy components, including: (1) work done by external forces, W_{ext}; (2) kinetic energy of the system, E_k; (3) strain energy, E_{strain}; (4) bond energy stored in parallel bonds, E_{pb}; (5) interparticle friction dissipation, E_f; and (6) damping energy of REAL, E_d. Any heat transmitted is ignored in the current DEM analysis. More details about these energy components can be found by O'Sullivan (2011) and Itasca (2020).

At a given hammer drop, the energy conservation law is satisfied:

$$W_{ext} = E_{strain} + E_k + E_{pb} + E_f + E_d \quad (9)$$

The work done by the applied impact forces can be determined in an increment form (ΔW_{ext}) by:

$$\Delta W_{ext} \leftarrow \Delta W_{ext} + \sum_{i=1}^{N_b}\left((m_i g + F_i)\Delta U_i + M_i \Delta\theta_i\right) \quad (10)$$

where, N_b, m_i, g, F_i, M_i, ΔU_i and $\Delta\theta_i$ are the number of ballast particles, gravitational mass, gravity acceleration (9.81 m/s^2), external forces, external moment, calculated displacement increment and calculated rotation increment, respectively.

The strain energy (E_{strain}) that is stored in the contacts between particles and dissipated through particle interactions and upon deformation is calculated from:

$$E_{strain} = \frac{1}{2}\sum_{i=1}^{N_c}\left(\frac{|F_i^n|^2}{k_n} + \frac{|F_i^s|^2}{k_s}\right) \quad (11)$$

where, N_c is the number of contacts; $|F_i^n|$ and $|F_i^s|$ are the magnitudes of the normal and shear forces, respectively.

The energy (E_k) that is accounted for both displacement and rotation of ballast aggregates is computed by (Itasca 2020):

$$E_k = \sum_{i=1}^{N_b}\left(\frac{1}{2}m_i V_i^2 + \frac{1}{2}I_i\omega_i \cdot \omega_i\right) \quad (12)$$

where, N_b, m_i , I_i , V_i and ω_i are the number of ballast particles, the mass, the inertia momentum, and the translational and rotational velocities of a given particle within the assembly, respectively.

Bond energy (E_{pb}) stored in parallel bonds is computed by (Potyondy and Cundall 2004):

$$E_{pb} = \frac{1}{2}\sum_{i=1}^{N_{pb}}\left(\frac{|\overline{F}_i^n|^2}{Ak_n} + \frac{|\overline{F}_i^s|^2}{Ak_s} + \frac{|\overline{M}_i^n|^2}{Jk_s} + \frac{|\overline{M}_i^s|^2}{Ik_n}\right) \quad (13)$$

where, N_{pb} is the number of parallel bonds; $\overline{F}_i^n$, $\overline{M}_i^n$ and $\overline{F}_i^s$, $\overline{M}_i^s$ denote the normal and shear components of forces and moments, respectively; and k_n and k_s are the normal and shear-contact stiffness. It is noted that when a parallel bond breaks, the accumulated bond energy (E_{pb}) will be lost, and this part of the energy loss is treated as the dissipation of breakage energy.

The energy that is dissipated by frictional slip (friction dissipation ΔE_f) is calculated in an incremental form as:

$$\Delta E_f = \sum_{i=1}^{N_c}\left(-\frac{1}{2}((F_i^s)_0 + F_i^s)\Delta\delta_s^\mu\right) \quad (14)$$

where, $(F_i^s)_0$, F_i^s are the contact shear forces at the beginning and the end of the timestep Δt; $\Delta\delta_s^\mu$ is the slippage component of the relative shear displacement between two contacted particles.

The damping energy (E_d) associated with the energy absorption of REAL and it is related to the elastic deformation of the REAL upon impact load. The E_d is proportional to the force (F_i^d) that transferred to the REAL layer and can be calculated in an incremental form, as given by:

$$\Delta E_d = -F_i^d(\dot{\delta} \,.\, \Delta t) \quad (15)$$

where, $\dot{\delta}$ is the rate of relative translational velocity and Δt is a timestep.

The implications of a damping coefficient (ζ) on energy calculations are that it influences damping force (F_i^d) applied to each particle and dissipated energy (ΔW), as given by:

$$F_i^d = -\zeta \left| F_i^d \right| sign(v_i) \quad \text{where} \quad sign(v) = \begin{cases} +1, & v > 0 \\ -1, & v < 0 \\ 0, & v = 0 \end{cases} \quad (16)$$

$\left| F_i^d \right|$ is the magnitude of the unbalanced force on the particle.

RESULTS AND DISCUSSION

Load-displacement responses

Measurements taken in laboratory tests include: impact forces, vertical settlements, lateral displacements, acceleration, and ballast breakage. A high-speed camera (500 frames per second, 1280 x 800 resolution) was used to record deflections during the impact loading. Samples of output signals of deflection and acceleration recorded from impact tests under drop heights, h_d = 150, 250 mm at N_{drop}=5 are presented in an Appendix B. It is noted that real-life measurements of track deflections and accelerations have been carried out worldwide. Indraratna *et al*. (2014) conducted field testing at a track in Singleton, NSW and reported the track settlements were found around 12-20mm after 500,000 loading cycles. Sadeghi *et al*. (2017b, 2018) carried out field tests on metro tracks, having a wide range of track stiffnesses and reported that track deflection and acceleration values vary significantly depending on the type of track structure.

Figure 7 shows a comparison between the predicted vertical settlement S_v (with and without REAL) obtained from the simulations, and those measured from the laboratory impact tests under drop heights of h_d = 150 mm, and 250 mm. The settlements are calculated from the position of the top-loading surface of the assembly for each drop. In general, the inclusion of REAL reduces ballast settlement, for instance, where h_d = 150 mm, the maximum vertical displacement after N_{drop}=15 with and without the inclusion of REAL is 65.18 mm and 74.23 mm, respectively. The predicted values of S_v generally match those obtained from the laboratory, and show a significantly increased settlement within the first eight hammer drops ($N_{drop} = 8$), followed by gradually increasing settlement until the end of the test ($N_{drop} = 15$). During the initial hammer drops, ballast aggregates undergo significant re-arrangement and compression, but after reaching some threshold densification, any subsequent impact loading would resist further compression and promote particle crushing and breakage.

It is noted that the total height of the layered track element (560 mm) of the ballast assembly was kept the same as for all tests with and without the inclusion of REAL (10 mm thick). While the thickness of the ballast layer and capping were unchanged, the thickness of the subgrade layer was increased from 50 mm to 60 mm to compensate for the absence of REAL (Fig. 1b). With this test setup, the effect of the sample height on the stiffness and the corresponding deflection can then be eliminated. The overall track stiffness (K) is a combination of stiffness from various track components (in a series form), and in the case of a ballast track the equivalent track stiffness can be calculated by (Powrie and Le Pen. 2016):

$$\frac{1}{K} = \frac{1}{k_{sleeper}} + \frac{1}{k_{ballast}} + \frac{1}{k_{REAL}} + \frac{1}{k_{capping}} + \frac{1}{k_{subgrade}} \qquad (17)$$

The stiffness of any substructure element (k) can be represented by the well-known expression, $k=EA/h$, where, E is the modulus of elasticity, A is the area, and h is the element height (thickness).

The above theoretical concepts indicate that any change in the material properties of the track components can result in a corresponding change in its overall stiffness. It is noted that the stiffness of REAL is lower than the stiffness of other track layers, hence, the inclusion of REAL may generally reduce the overall track stiffness thus effecting a potential increase in settlement. However, as the thickness of REAL is only 10mm, this may not significantly influence the overall track stiffness. Moreover, due to the relatively high energy energy-absorbing capacity of rubber, the inclusion of REAL would result in a significant reduction of ballast degradation, hence contributing to a reduction in track settlement.

After each hammer drop, the circumference of ballast assemblies was measured at the top, middle, and bottom of the ballast layers (locations: A, B, C) to determine lateral displacements, as shown in Figure 8. Measured data show that with the inclusion of REAL, lateral deformation of ballast decreases for any given drop height, h_d and this is because of the energy absorbing capacity of REAL. The lateral displacements increase with successive impacts, but the rate of increment gradually decreases after the 8^{th} drop. The initially rapid lateral displacement of ballast could be attributed to the high rate of ballast breakage that occurs at this stage.

Figure 9 shows the evolution of lateral displacement contours of a ballast assembly subjected to a hammer drop height of h_d = 150 mm. The total lateral displacements (L_d) are determined by averaging the circumference of the ballast assembly at 3 locations (top, middle and bottom). It is seen that the predicted values of L_d increase with an increase in the number of hammer drops (N_{drop}), and the inclusion of REAL decreases the lateral deformation of the ballast specimens. The predicted lateral displacements of ballast agree well with the test data measured by Ngo *et al.* (2019). The ballast assembly without the inclusion of REAL exhibits a maximum lateral displacement of about L_d = 58.5 mm compared to L_d = 51.4 mm for the reinforced case. A more obvious beneficial effect of the REAL in reducing lateral deformation of ballast can be found when the number of drop $N_{drop} \geq 5$. For instance, at N_{drop}=5 the ballast assembly without the inclusion of REAL exhibits a lateral displacement of about L_d = 40.8 mm compared to L_d = 30.6 mm for the reinforced case, indicating an approximately of 25% reduction. When the N_{drop} increases to 10th and 15th drop, the reduction in lateral deformation of ballast attributed to the inclusion of REAL is around 15% and 12%, respectively, which can clearly demonstrate the effect of the REAL.

To further explore the effect of REAL on the ballast deformation from a micromechanical perspective, the displacement vectors of ballast (with and without the presence of REAL) are captured at the hammer drops of N_{drop} =5th and 15th, as shown in Figure 10. Actually deformed ballast assemblies taken by high-speed camera at the N_{drop} =5th are included for comparison. It is evident that upon impact loads, particles in the specimen without REAL (Fig. 10a) tend to move horizontally leading to increased lateral displacement, as measured experimentally. In contrast, with the inclusion of REAL, particles displace more downward forming more contacts at the bottom layer of ballast leading to reduced lateral deformation. This can be attributed to the REAL is modelled as an elastic media with a much lower stiffness as compared to that of the ballast layer and the damping property of the REAL, which in essence could act as a shock absorber underneath the ballast layer, creating increased contact areas between particles and the REAL. It is noted that without REAL, these particles may have directly made contact with the very stiff capping layer, which may have then caused them to displace laterally. This micro-analysis supports the deformation mode of lateral bulging as observed in the laboratory (Fig. 10a).

Role of REAL on the impact forces

Figure 11 shows the comparison between the impact forces predicted from the simulations with those measured in the laboratory, with and without REAL, for a given drop height of h_d =150 mm. The data points are reported during the first 200 (ms) and recorded at N_{drop} = 8. It is seen that the predicted time histories of impact forces are similar to those measured experimentally, having multiple short peaks (P_1 force), followed by a much longer duration of a less prominent peak of smaller magnitude (P_2 force). When the hammer impacts the ballast assembly, the first peak (P_1) occurs as the specimen accelerates to the speed of the hammer, producing a high inertial force. The predicted impact forces show that the first peak has a sharp triangular shape that represents a high amplitude of about 247 kN for a very short time of about 10 ms. Multiple second peaks are then observed after the first peak, followed by several sharp peaks, before the impact forces decrease to around 30 kN at the end of the impact. While the inclusion of REAL produces a similar trend for the impact forces, it significantly decreases the magnitude of the impact forces (P_1). A maximum impact force is measured at about 247 kN (without REAL), and this value decreases to about 158 kN (with REAL), thus showing an approximately 36% reduction in impact forces attributed to the inclusion of REAL.

Comprehensive field measurements carried out by Indraratna *et al*. (2010, 2014) in the towns of Bulli and Singleton in the state of NSW have shown that under the passage of a coal train with 100 tonne wagons (i.e. 25-tonne axle load), the maximum vertical cyclic stresses were measured in the proximity of 230 kPa. However, one peak observed at 415 kPa was found to be caused by a wheel-flat generating an impact force. In the field, the wheel load is transmitted both vertically (underneath sleepers) and laterally to adjacent sleepers, and around 40-60% of the wheel load is carried by the sleeper directly beneath the wheel (Atalar et al. 2001, Chandra 2007). It is noted that the type of impact testing carried out in this study may not perfectly simulate the field conditions as the spreading of load between adjacent sleepers could not be considered. Nevertheless, the drop heights and drop mass were selected to produce vertical stresses in the range of σ_1=300-600 kPa, to simulate typical impact forces caused by wheel flats and dipped rail joints as measured in the field and explained elsewhere by Remennikov and Kaewunruen (2014) and Indraratna et al. (2010).

Role of REAL on the contact force distribution

Subjected to impact forces from hammer drops, a network of contact force-chain develops across the ballast particles to resist the applied forces and transfer them to the underlying layers. The orientation of contact force distribution varies with the applied loads and directly governs the deformation and strength of a discrete granular assembly (Oda and Iwashita 1999, Guo *et al.* 2020). Altuhafi *et al.* (2016) showed that the amount of particle breakage should depend not only on the strength of the particle but also on the distribution of contact forces and arrangement of particles. Figure 12 shows the evolution of inter-particle contact forces that develops in the ballast and the vertical stress contours in the capping/subgrade layers captured at hammer drops where N_{drop} = 1, 5, 10 and 15. Each contact force is shown at the point of contact in the direction of the particle centroid, where its thickness is proportional to the intensity of the contact force. It is observed that the force distribution in the DEM region is heterogeneous (non-uniformly distributed), where the number of contacts ($N_{contact}$) and maximum contact forces (F_{max}) change with increased N_{drop}. At any given hammer drop, the inclusion of REAL decreases the maximum contact forces due to the energy absorbing property of REAL; this causes less impact forces to be transferred to the ballast aggregates. In fact, at N_{drop} =1, unreinforced ballast (without REAL) shows a maximum contact force of F_{max} = 781N, while the reinforced ballast (with REAL) shows a lower contact force of F_{max} = 675N. The inclusion of REAL also increases the number of contacts ($N_{contact}$ =1298 and 1429 for unreinforced and reinforced assemblies, respectively). Most of the high contact forces are found at the top ballast layer (underneath the rigid loading plate) where they directly support the impact loads. As the impact test progresses to the final drop (N_{drop} =15), the contact forces intensify and reach a value of F_{max}=688N and 798N for tests with and without the inclusion of REAL, respectively. The increased F_{max} with the subsequent increase in N_{drop} can be attributed to the increased packing density of the specimen and particle breakage. The vertical stress contours (σ_{zz}) on the continuum substructure (REAL, capping and subgrade) are also captured in the coupled discrete-continuum simulation. The vertical stress has a maximum value of about 100 kPa in the capping layer, and then it decreases with depth, as expected.

To further explore the effect of REAL from a micromechanical perspective, the evolutions of the number of contacts, $N_{contact}$ and maximum contact forces, F_{max} predicted from DEM for ballast assemblies with and without REAL are presented in Figure 13. It is seen that while the $N_{contact}$ increases significantly with the inclusion of REAL, the maximum value of contact forces decreases. When a rubber mat such as REAL is placed beneath the ballast, the applied impact loads do not only transmit through the large aggregate skeleton but also transfer across the rubber mat and particles. This results in a reduced maximum contact force magnitude contacts (i.e., with REAL: F_{max}=675-688 N; without REAL: F_{max}=775-810 N) corresponding to a higher number of particle contacts (i.e., with REAL: $N_{contact}$ =1314-1429; without REAL: $N_{contact}$ =1245-1298). The significant energy absorption capacity by the REAL diminishes the effects of high-impact loads and attenuates the transmission of impact-induced shocks effectively, thereby reducing the track deformation. The REAL increases $N_{contact}$ and this is attributed to the increased contact area (more particles are effectively allowed to contact with REAL), whereas the energy absorbing capacity of the REAL results in reduced F_{max}. The vertical distribution of contact forces is affected by the REAL, with more horizontal 'locked in' forces towards the bottom of the sample. This indicates that the impact load has been distributed more evenly along the capping and subgrade layer, hence preventing the damage due to stress concentrations. As a result, particle breakage is decreased due to diminishing the intensity of contact forces concentrated in the ballast matrix. This micro-level analysis of DEM provides insightful information about the effect of REAL which is not actually possible to measure in laboratory testing.

Capturing ballast breakage

One of the most challenging issues related to DEM analysis is to consider particle breakage and complex particle shape at the same time, where these aspects are often ignored by the conventional continuum modelling approach. The angularity of ballast particles are modelled by parallel bonds (Fig. 5a); the breaking of these bonds can be considered to represent particle breakage (Cheng *et al.* 2004, Ciantia *et al.* 2015, Li and McDowell 2018). Although this method cannot predict the breakage quantitatively as experienced in real-life track conditions, it successfully modelled the effect of REAL on ballast breakage and provided relatively fast computational speed. The maximum tensile (σ_{max}) and shear stresses (τ_{max}) acting on each bond are determined by (Potyondy and Cundall 2004):

$$\sigma_{max} = \frac{-\overline{F}_i^n}{A} + \frac{\left|\overline{M}_i^s\right|}{I}\overline{R}\ ; \quad \text{and } \tau_{max} = \frac{\left|\overline{F}_i^s\right|}{A} + \frac{\left|\overline{M}_i^n\right|}{J}\overline{R} \qquad (18)$$

where, A, J and I are the area, and the polar and inertia moments of the bond cross-section, respectively. If either of these maximum stresses exceeds its corresponding bond strength, the bond breaks (Russell *et al.* 2009). Figure 14 presents snapshots of the evolution of broken bonds captured during the impact tests (h_d = 200mm), for ballast assemblies with and without REAL. It is seen that most of the broken bonds occur just under the loading plate (top layer of ballast), and this observation agrees with the ballast breakage measured in the laboratory. After repeated hammer drops, a concentration of particle breakage occurs beneath the loading plate, and there are a small number of broken bonds at the bottom of the ballast layer. An increasing number of hammer drops (increased N_{drop}) results in an increased number of broken bonds ($N_{Breakage}$) and the breakage starts occurring in the bottom ballast layer ($N_{Breakage}$ = 45 and 374 at N_{drop}=1 and 15, respectively). However, the inclusion of REAL significantly decreases $N_{Breakage}$ by about 34% (i.e., at N_{drop}=15: $N_{Breakage}$ = 248 with REAL compared to $N_{Breakage}$ = 374 without REAL). The reduced $N_{Breakage}$ associated with REAL is because it could distribute the load over a wider area and attenuate the dynamic forces, apart from retaining the energy is transferred to the surrounding ballast aggregates. It is noted that the interface/contact conditions between the steel loading plate and ballast aggregates were tested in this study representing a hard surface of concrete sleepers in practice, albeit this caused breakage of corner and sharp edges of ballast. To mitigate this issue, an elastic element (Under Sleeper Pad -USP) can be utilised, and this will be carried out in the future study.

Figure 15 shows accumulated broken bonds ($N_{Breakage}$) with an increased number of hammer drops (N_{drop}) under a drop height of h_d = 150 mm, with and without REAL. The actual amount of ballast breakage index (BBI) measured in the laboratory is also presented for comparison. It is observed that $N_{Breakage}$ increases with an increase in the N_{drop}, while the inclusion of REAL results in a significant decrease in $N_{Breakage}$. The increased values of $N_{Breakage}$ with an increase in N_{drop} agrees with the ballast breakage index (BBI) measured in the laboratory. The reduction in $N_{Breakage}$ is believed to be due to the energy absorbing property of REAL, which means less impact energy is transferred to the aggregates and there is less breakage. Furthermore, REAL provides a better distribution of applied impact forces over wider areas, which reduces the contact forces, as shown in Fig. 12b.

Variation of coordination number

The coordination number (C_n) is an important microscopic parameter in describing the packing of particles and can be determined as the average number of contacts per particle for a given volume (Soga and O'Sullivan 2010, Ciantia *et al.* 2019). The change in C_n is an indication of loss or generation of contacts, it depends not only on the change of packing density, but also on the rate of newly-formed contacts and particle breakage. Hasan and Alshibli (2010) found that C_n is linked to the contact force networks and the load-carrying capacity of a granular assembly. Todisco *et al.* (2015) studied the effect of the coordination number on particle crushing and proved that particles compressed with higher value of C_n have a lower likelihood of breaking. Figure 16 shows the variation of coordination number C_n with an increased number of N_{drop} subjected to drop heights where h_d =100 and 200 mm. It is seen that although C_n decreases with the number of hammer drops as the aggregates displace and break into smaller grains, the value of C_n exhibits a slight increase with increased N_{drop} towards the end of the test. With the inclusion of REAL, C_n shows a relatively constant value of about 6.62 throughout testing, but without REAL, C_n exhibits significant fluctuations (varying from 6.35 to 6.6), which could be associated with the breakage causing the particles to be re-arranged, displaced and forming new contacts to support the induced impact load. The inclusion of REAL results in a slightly higher value of C_n (i.e. C_n = 6.62 with REAL compared to C_n = 6.51 without it). The variations of C_n can be used to reflect the ability of the ballast assembly to maintain its current configuration because a higher value of C_n imposes more restraints on particle displacement and breakage.

Evolution of energy components

Figure 17 shows the energy components of a ballast assembly captured after the first hammer drop (N_{drop} = 1) with the inclusion of REAL and subjected to a given drop height of h_d = 100 mm. When the hammer starts to drop, the kinetic energy of the whole system (E_k) accelerates and reaches a maximum value of E_k = 761 J as soon as the hammer hits the ballast, and this is followed by a significant reduction as the E_k is transferred to other energy components once the hammer is at rest. By contrast, the component of strain energy (i.e., the internal particle deformation) increases to the highest value of E_{strain}= 523 J when the hammer touches the specimen and fluctuates to around 385 J at the end of the first drop. This strain energy E_{strain} increases rapidly during the impact as a result of the work performed on the ballast assembly (i.e., ballast deformation). Similarly, the energy dissipated through the friction (slippage), E_f also experiences a considerable increase when the hammer drops onto the ballast assembly. Unlike E_{strain} which has some fluctuations (Fig. 17), E_f remains relatively unchanged and it reaches a value of about E_f = 221 J at the end of the first drop. Here, the bond energy steadily increases to a value of E_{pb} = 64.8 J, albeit with some fluctuations as this energy dissipates when the bond of the cluster of particles breaks. The damping energy absorbed by REAL can be calculated with respect to the damping forces, and the amount of rubber compression that had occurred during impact load. Here, the energy absorption of REAL consistently increases during the first hammer drop and reaches a final value of around E_d = 107 J. The dissipated energy, by either damping or slippage, increases throughout the hammer drop, as expected.

To further investigate the energy absorbing capacity of recycled rubber mats, comparisons of the energy components (with and without REAL) subjected to h_d =150 mm captured at different N_{drop} is shown in Figure 18. The inclusion of REAL reduces the frictional slip energy and decreases the strain energy, E_{strain} (maximum value of E_{strain} = 931 J, compared to E_{strain} =1062 J without REAL); this leads to a reduction in ballast deformation, as measured in the laboratory. In general, all the accumulated energy components increase as the number of hammer drops increase (N_{drop}), except for the energy absorbed by the rubber mat (E_d) remains almost unchanged after N_{drop} = 5. This could be due to the rubber mat being compressed to its approximate limit after 5 drops. The effect of REAL has been demonstrated by considering the increased energy dissipated through damping (i.e., E_d = 425 J and 139 J with and without REAL, respectively). In contrast, the energy stored by the parallel bonds E_{pb} is lower when REAL is included (i.e., E_{pb} = 189 J with REAL, compared to E_{pb} = 285 J without REAL), and this could explain the reduced number of broken bonds (Fig. 15). When a bond is broken, some of the bond energy is dissipated due to particle breakage, this also causes fluctuations in the coordination number (Fig. 16). Figure 18 also reveals that without the inclusion of REAL, friction-related energy dissipation dominates the amount of energy consumed by the impact load, whereas damping-related dissipation takes a secondary role (E_f =795 J, E_d =212J). However, with the inclusion of REAL, the damping energy of the ballast assembly increased up to about E_d =412 J and the energy dissipated by frictional slip dropped to around E_f= 597 J.

Limitations and future study

The main objective of this study was to introduce an innovative application of a recycled rubber mat in reducing the deformation and breakage of ballast that has been tested both experimentally and numerically. Nevertheless, there are certain limitations in the current analysis that need to be considered for future study, as follows:

- The breakage of bonds at best can only be considered a proxy measure of particle damage using parallel bonds. Although this method cannot predict the breakage quantitively as the particles cannot continue to break, it successfully modelled the effect of REAL on ballast breakage and provided relatively fast computational speed. A more advanced contact model (i.e., Conical Damage Model introduced recently by Suhr *et al.* 2022) may be adopted to capture more realistic particle breakage.

- A more comprehensive future work of parametric study concerning the REAL (having different thicknesses and varied stiffnesses) and foundation (capping and subgrade) characteristics covering a wide range of geotechnical soil conditions will allow addressing optimisation conditions of the use of REAL.

- To promote sustainable solutions in railway tracks, it is recommended to test the effectiveness of a potential combination of using under sleeper pads (USP) and REAL techniques and evaluate their performance in tracks at critical scenarios (e.g., transition zones, railway crossings).

CONCLUSIONS

The role that recycled rubber mats manufactured from waste tyres has on reducing the deformation and degradation (breakage) of ballast was analysed in this study. A series of drop-weight impact tests were carried out in the laboratory to evaluate the improved performance of ballast when recycled rubber mats were used. Numerical modelling was performed using the coupled discrete-continuum modelling approach to understand the complex interaction of discrete ballast grains and continuum media (rubber mat, subgrade). The outcomes of this study provide more insights on the role of REAL in terms of particle breakage, distribution of contact forces, number of contacts, maximum contact forces, and evolution of coordination number (C_n), none of which could be captured purely based on laboratory testing. The following specific conclusions can be drawn:

- Laboratory test data and numerical simulations showed that the inclusion of REAL attenuated the settlement and lateral deformation of ballast, as well as particle breakage under impact loading. Subjected to a drop height of h_d = 150 mm, the maximum settlement measured at N_{drop}=15 with and without the inclusion of REAL was S_v=65.18 mm 74.23 mm, respectively. A maximum lateral displacement of ballast with REAL was found at L_d = 51.4 mm compared to L_d = 58.5 mm for the ballast assembly without REAL. These observations prove without a doubt that REAL effectively controls both the vertical and lateral deformations of the ballast layer.

- The variation in the number of contacts predicted from DEM analysis showed that the presence of REAL resulted in increased $N_{contact}$ (with REAL: $N_{contact}$ =1314-1429; without REAL: $N_{contact}$ =1245-1298). When a rubber mat was placed beneath the ballast, the impact loads did not only transmit through the large aggregate skeleton but also transfered across the rubber mat and particles leading to a higher number of contacts and affecting the particle displacement vectors. This finding provided an insight into force transmission in the granular matrix which was not really possible to measure in the experimental tests.
- Results from the DEM analysis demonstrated that the REAL decreased the maximum contact force F_{max}. In fact, at N_{drop} =1, the ballast without REAL showed F_{max} = 781 N while the ballast with REAL showed a lower value of F_{max} = 675 N. This result implied that the energy absorbing property of REAL contributed to less impact forces transferred to the ballast aggregates, hence preventing ballast breakage due to stress concentration.
- From numerical results, it was evident that the REAL significantly reduced the number of broken bonds, $N_{Breakage}$ by up to about 34% (for instance, at N_{drop}=15: $N_{Breakage}$ = 248 with

REAL, compared to $N_{Breakage}$ = 374 without REAL). Also, REAL helped to increase the coordination number C_n (i.e., C_n = 6.62 with REAL, compared to C_n = 6.51 without REAL). These simulation results implied that the higher value of C_n would impose more restraint on particle displacements and associated breakage.

- The effect of the energy absorbing layer (REAL) was demonstrated by considering the substantially increased energy dissipation attributed to damping (E_d = 425 J and 139 J with and without REAL, respectively). Moreover, REAL helped to decrease the frictional slip energy (reduced slippage) and to reduce the strain energy (with REAL, the maximum value of E_{strain} = 931 J, compared to E_{strain} =1062 J without REAL), thereby reducing the ballast deformation as measured in the laboratory.

ACKNOWLEDGEMENTS

This study was carried out by the Industrial Transformation Training Centre for Advanced Technologies in Rail Track Infrastructure (ITTC-Rail), funded by the Australian Research Council, ARC (IC170100006) and the ARC Discovery Project (DP220102862). The authors appreciate the insightful collaboration and assistance of Australian Rail Track Corporation (ARTC), Transport for NSW, Australasian Centre for Rail Innovation (ACRI), SMEC and MTM for their continuous cooperation and support. The authors are grateful to Professor David Potts at Imperial College London who provided valuable insight to computational complexities during the term of ITTC-Rail. The authors are thankful to Professor Glenn McDowell, University of Nottingham who provided valuable discussions during his involvement with the authors in a past related ARC Discovery project.

APPENDIX A

The continuum FDM zone is divided into segments where each vertex corresponds to the element node. As shown in Figure 19, a continuum element (length, L) is in contact with a discrete ballast particle, j (contact location, $\overrightarrow{C_p}$), where L_1 and L_2 are the distances of the contact point to vertex (i) and vertex ($i+1$), having corresponding vector positions of $\vec{v}_i$, and $\vec{v}_{i+1}$. Then:

$$L_1 = d(\overrightarrow{C_p}, \vec{v}_i) = \sqrt{\left(C_1 - v_{(i)_1}\right)^2 + \left(C_2 - v_{(i)_2}\right)^2} \quad (19)$$

$$L_2 = d(\overrightarrow{C_p}, \vec{v}_{i+1}) = \sqrt{\left(C_1 - v_{(i+1)_1}\right)^2 + \left(C_2 - v_{(i+1)_2}\right)^2} \quad (20)$$

Assume the element has a relative angle to horizontal direction of Φ, then:

$$\Phi = tan^{-1}\left[\frac{v_{(i)_1} - v_{(i+1)_1}}{v_{(i)_2} - v_{(i+1)_2}}\right] \quad (21)$$

Therefore, for $\Phi \neq 0$:

$$L_{1x} = L_1 \times cos\Phi \; ; \quad \text{and: } L_{1y} = L_1 \times sin\Phi \quad (22)$$

$$L_{2x} = L_2 \times cos\Phi \; ; \quad \text{and: } L_{2y} = L_2 \times sin\Phi \quad (23)$$

Contact forces of ballast particle, j (F_{xj} and F_{yj}) are divided into horizontal and vertical forces at each wall vertex, described as:

$$\begin{cases} f_{xj(i)} = \frac{F_{xj} \times L_{2x}}{L_x} \\ f_{yj(i)} = \frac{F_{yj} \times L_{2y}}{L_y} \end{cases} \quad (24)$$

$$\begin{cases} f_{xj(i+1)} = \frac{F_{xj} \times L_{1x}}{L_x} \\ f_{yj(i+1)} = \frac{F_{yj} \times L_{1y}}{L_y} \end{cases} \quad (25)$$

In case of $\Phi = 90^o$:

$$L_{1x} = L_1 \times cos\Phi = L_1; \quad \text{and: } L_{1y} = L_1 \times sin\Phi = L_1 \quad (26)$$

$$L_{2x} = L_2 \times cos\Phi = L_2; \quad \text{and: } L_{2y} = L_2 \times sin\Phi = L_2 \quad (27)$$

hence:

$$\begin{cases} f_{xj(i)} = \frac{F_{xj} \times L_2}{L_x} \\ f_{yj(i)} = \frac{F_{yj} \times L_2}{L_y} \end{cases} \quad (28)$$

$$\begin{cases} f_{xj(i+1)}=\frac{F_{xj}\times L_1}{L_x} \\ f_{yj(i+1)}=\frac{F_{yj}\times L_1}{L_y} \end{cases} \tag{29}$$

The forces calculated at the vertex are transferred into an equivalent element node and the corresponding nodal velocities are transferred to DEM zone as input boundary conditions. In this way a full coupling between the discrete and continuum zones can be performed.

APPENDIX B

Samples of output signals of deflection and acceleration recorded from impact tests under drop heights, h_d = 150, 250 mm at N_{drop}=5 recorded for ballast assemblies with and without the inclusion of REAL are presented in Figure 20.

REFERENCES

Data Availability Statement

Some or all data used are available from the corresponding author by request.

Altuhafi, F. N., Coop, M. R. and Georgiannou, V. N. (2016). Effect of Particle Shape on the Mechanical Behavior of Natural Sands. *Journal of geotechnical and geoenvironmental engineering* 142(12): 4016071.

Alves Costa, P., Calçada, R. and Silva Cardoso, A. (2012). Ballast mats for the reduction of railway traffic vibrations. Numerical study. *Soil Dynamics and Earthquake Engineering* 42: 137-150.

Anastasopoulos, I., Alfi, S., Gazetas, G., Bruni, S. and Leuven, A. V. (2009). Numerical and Experimental Assessment of Advanced Concepts to Reduce Noise and Vibration on Urban Railway Turnouts. *Journal of Transportation Engineering* 135(5): 279-287.

AS_2758.7: (2015). Aggregates and rock for engineering purposes, Part 7. *Railway Ballast. Standard Australia* NSW, Australia.

Atalar, C., B. M. Das, E. C. Shin and D. H. Kim (2001). Settlement of geogrid-reinforced railroad led to failure due to cyclic load. *Proceedings of the 15th International Conference on Soil Mechanics and Geotechnical Engineering*, Istanbul.

Auersch, L. (2006). Dynamic Axle Loads on Tracks with and Without Ballast Mats: Numerical Results of Three-Dimensional Vehicle-Track-Soil Models. *Proceedings of the Institution of Mechanical Engineers, Part F: Journal of Rail and Rapid Transit* 220(2): 169-183.

Bathurst, R. J. and Raymond, G. P. (1987). Geogrid reinforcement of ballasted track. *Transportation Research Record* 1153: 8-14.

Biabani, M. M., Indraratna, B. and Ngo, N. T. (2016). Modelling of geocell-reinforced subballast subjected to cyclic loading. *Geotextiles and Geomembranes* 44(4): 489-503.

Bolton, M. D., Nakata, Y. and Cheng, Y. P. (2008). Micro- and macro-mechanical behaviour of DEM crushable materials. *Geotechnique* 58(6): 471–480.

Breugnot, A., Lambert, S., Villard, P. and Gotteland, P. (2016). A Discrete/continuous Coupled Approach for Modeling Impacts on Cellular Geostructures. *Rock Mechanics and Rock Engineering* 49(5): 1831-1848.

Brown, S. F., Kwan, J. and Thom, N. H. (2007). Identifying the key parameters that influence geogrid reinforcement of railway ballast. *Geotextiles and Geomembranes* 25(6): 326-335.

Chandra, S., 2007. Railway engineering. Oxford University Press, UK.

Chen, C., McDowell, G. R. and Thom, N. H. (2013). A study of geogrid-reinforced ballast using laboratory pull-out tests and discrete element modelling. *Geomechanics and Geoengineering* 8(4): 244-253.

Cheng, Y. P., Bolton, M. D. and Nakata, Y. (2004). Crushing and plastic deformation of soils simulated using DEM. *Géotechnique* 54(2): 131-141.

Chumyen, P., D. Connolly, P. Woodward and V. Markine (2022). The effect of soil improvement and auxiliary rails at railway track transition zones. *Soil Dynamics and Earthquake Engineering*. 155: 107200.

Ciantia, M. O., Arroyo, M., Calvetti, F. and Gens, A. (2015). An approach to enhance efficiency of DEM modelling of soils with crushable grains. *Géotechnique* 65(2): 91-110.

Ciantia, M. O., Arroyo, M., O'Sullivan, C. and Gens, A. (2019). Micromechanical inspection of incremental behaviour of crushable soils. *Acta Geotechnica* 14(5): 1337-1356.

Connolly, D.P., Kouroussis, G., Woodward, P.K., Costa, P.A., Verlinden, O. and Forde, M.C., 2014. Field testing and analysis of high speed rail vibrations. *Soil Dynamics and Earthquake Engineering*, *67*, pp.102-118.

Cundall, P. A. and Strack, O. D. L. (1979). A discrete numerical model for granular assemblies. *Geotechnique* 29(1): 47-65.

DIN (2010). Mechanical vibration—Resilient elements used in railway tracks. Part V: Laboratory test procedures for under-ballast mats. *45673–5, Berlin*.

Esmaeili, M.H., Norouzi, H. and Niazi, F., (2023). Evaluation of mechanical and performance characteristics of a new composite railway sleeper made from recycled plastics, mineral fillers and industrial wastes. *Composites Part B: Engineering*, *254*, p.110581.

Esveld, C. (2014). Modern railway track, MRT Press, The Netherlands.

Giroud, J. P. and Han, J. (2004). Design method for geogrid-reinforced unpaved roads. I. Development of design method. *Journal of Geotechnical and Geoenvironmental Engineering* 130(8): 775-786.

Guo, Y., Zhao, C., Markine, V., Jing, G. and Zhai, W. (2020). Calibration for discrete element modelling of railway ballast: A review. *Transportation Geotechnics* 23: 100341.

Hanson, C.E. and Singleton Jr, H.L. (2006). Performance of ballast mats on passenger railroads: Measurement vs. projections. *Journal of Sound and Vibration,* 293(3–5), pp: 873-877.

Hasan, A. and Alshibli, K. A. (2010). Experimental assessment of 3D particle-to-particle interaction within sheared sand using synchrotron microtomography. *Géotechnique* 60(5): 369-379.

Huang, H. and Tutumluer, E. (2011). Discrete Element Modeling for fouled railroad ballast. *Construction and Building Materials* 25: 3306-3312.

Indraratna, B., S. Nimbalkar, D. Christie, C. Rujikiatkamjorn and J. S. Vinod (2010). Field assessment of the performance of a ballasted rail track with and without geosynthetics. *Journal of Geotechnical and Geoenvironmental Engineering*. 136(7): 907–917.

Indraratna, B., Ngo, N. T. and Rujikiatkamjorn, C. (2011). Behavior of geogrid-reinforced ballast under various levels of fouling. *Geotextiles and Geomembranes* 29(3): 313-322.

Indraratna, B., Ngo, N. T. and Rujikiatkamjorn, C. (2013). Deformation of coal fouled ballast stabilized with geogrid under cyclic load. *Journal of Geotechnical and Geoenvironmental Engineering* 139(8): 1275-1289.

Indraratna, B., S. Nimbalkar and T. Neville (2014). Performance assessment of reinforced ballasted rail track. Proceedings of the Institution of Civil Engineers - Ground Improvement. 167(1): 24-34.

Indraratna, B. and Ngo, T. (2018). Ballast Railroad Design: Smart-Uow Approach, CRC Press.

Indraratna, B., Qi, Y., Ngo, T. N., Rujikiatkamjorn, C., Neville, T., Ferreira, F. B. and Shahkolahi, A. (2019). Use of geogrids and recycled rubber in railroad infrastructure for enhanced performance. *Geosciences* 9(1):30.

Itasca (2020). Particle flow code in three dimensions (PFC3D). *Itasca Consulting Group, Inc., Minnesota*.

Jia, W., V. Markine, M. Carvalho, D. P. Connolly and Y. Guo (2023). Design of a concept wedge-shaped self-levelling railway sleeper. *Construction and Building Materials*. 386: 131524.

Jia, W., V. Markine and Y. Guo (2023). Efficiency analysis and optimisation of DEM for railway ballast track simulations: Multi-layer shape model of lateral resistance. *Transportation Geotechnics*. 40: 100977.

Jiang, M. J., Yu, H. S. and Harris, D. (2005). A novel discrete model for granular material incorporating rolling resistance. *Computers and Geotechnics* 32: 340–357.

Konietzky, H., te Kamp, L. and Groeger, T. (2004). Use of DEM to model the interlocking effect of geogrids under static and cyclic loading. Numerical Modeling in Micromechnics via Particle Methods.

Le Pen, L., Milne, D., Thompson, D. and Powrie, W. (2016). Evaluating railway track support stiffness from trackside measurements in the absence of wheel load data. *Canadian Geotechnical Journal* 53(7): 1156-1166.

Le Pen, L., Watson, G., Hudson, A. and Powrie, W. (2018). Behaviour of under sleeper pads at switches and crossings–Field measurements. *Proceedings of the Institution of Mechanical Engineers, Part F: Journal of rail and rapid transit* 232(4): 1049-1063.

Leshchinsky, B. and Ling, H. I. (2013). Numerical modeling of behavior of railway ballasted structure with geocell confinement. *Geotextiles and Geomembranes* 36(2013): 33-43.

Li, H. and G. R. McDowell (2018). Discrete element modelling of under sleeper pads using a box test. *Granular matter*. 20(2): 26-26.

Lim, N.-H., K.-J. Kim, H.-U. Bae and S. Kim (2020). DEM Analysis of Track Ballast for Track Ballast–Wheel Interaction Simulation. *Applied Sciences*. 10(8): 2717.

Lim, W. L. and McDowell, G. R. (2005). Discrete element modelling of railway ballast. *Granular Matter* 7(1): 19-29.

Lobo-Guerrero, S. and Vallejo, L. E. (2005). Crushing a weak granular material: experimental numerical analyses. *Géotechnique* 55(3): 245–249.

McDowell, G. R., Harireche, O., Konietzky, H., Brown, S. F. and Thom, N. H. (2006). Discrete element modelling of geogrid-reinforced aggregates. *Proceedings of the ICE - Geotechnical Engineering* 159(1): 35-48.

Mondragon-Enguidanos, C., Verdú-Vázquez, A., Gil-López, T. and Gomez-Hoyos, J., 2021. Mechanical characterization of an elastomer made from end-of-life tires for its application in indirect railway fastenings. *Journal of the Brazilian Society of Mechanical Sciences and Engineering*, *43*(6), p.319.

Moubeké, C. A., Nguessong-Nkenfack, A., Ntamack, G. E., Beda, T. and Charif D'Ouazzane, S. (2021). Influence of Under Sleepers Rubber Mat on Propagation of Vibrations from a Railway Track Lying on a Semi-Infinite Soft Ground. *Indian Geotechnical Journal*.

Müller, R. (2008). Mitigation measures for open lines against vibration and ground-borne noise: A Swiss overview. *Noise and Vibration Mitigation for Rail Transportation Systems*, Springer Berlin Heidelberg, 610 264-270

Navaratnarajah, S. K. and B. Indraratna (2017). Use of rubber mats to improve the deformation and degradation behavior of rail ballast under cyclic loading. *Journal of Geotechnical and Geoenvironmental Engineering*. 143(6): 04017015.

Navaratnarajah, S. K., Indraratna, B. and Ngo, N. T. (2018). Influence of Under Sleeper Pads on Ballast Behavior Under Cyclic Loading: Experimental and Numerical Studies. *Journal of Geotechnical and Geoenvironmental Engineering* 144(9): 04018068.

Nimbalkar, S., B. Indraratna, S. K. Dash and D. Christie (2012). Improved Performance of Railway Ballast under Impact Loads Using Shock Mats. *Journal of Geotechnical and Geoenvironmental Engineering*. 138(3): 281-294.

Ngo, T. N., Indraratna, B. and Rujikiatkamjorn, C. (2019). Improved performance of ballasted tracks under impact loading by recycled rubber mats. *Transportation Geotechnics* 20: 100239.

Ngo, T. and B. Indraratna (2020). Mitigating ballast degradation with under-sleeper rubber pads: Experimental and numerical perspectives. *Computers and Geotechnics*. 122: 103540.

O'Sullivan, C. (2011). Particulate Discrete Element Modelling: A Geomechanics Perspective, Spon press, London.

O'Sullivan, C. and Cui, L. (2009). Micromechanics of granular material response during load reversals: Combined DEM and experimental study. *Powder Technology* 193(3): 289–302.

Oda, M. and Iwashita, K. (1999). Mechanics of granular materials: An introduction, Rotterdam: A. A. Balkema.

Potyondy, D. O. and Cundall, P. A. (2004). A bonded-particle model for rock. *International Journal of Rock Mechanics and Mining Sciences* 41(8): 1329-1364.

Powrie, W., and L. Le Pen. 2016. A guide to track stiffness. Southampton, UK: Uni. of Southampton.

Perez, J.L., Kwok, C.Y. and Senetakis, K., (2017). Micromechanical analyses of the effect of rubber size and content on sand-rubber mixtures at the critical state. *Geotextiles and Geomembranes*, 45(2): 81-97.

Priest, J. A., Powrie, W., Yang, L., Grabe, P. J. and Clayton, C. R. I. (2010). Measurements of transient ground movements below a ballasted railway line. *Géotechnique* 60(9): 667–677.

Raymond, G. and Ismail, I. (2003). The effect of geogrid reinforcement on unbound aggregates. *Geotextiles and Geomembranes* 21(6): 355-380.

Ramos, A., Gomes Correia, A., Calçada, R. and Alves Costa, P., (2022). Stress and permanent deformation amplification factors in subgrade induced by dynamic mechanisms in track structures. *International Journal of Rail Transportation*, 10(3): 298-330.

Remennikov, A. M. and Kaewunruen, S. (2014). Experimental load rating of aged railway concrete sleepers. *Engineering Structures* 76: 147-162.

Russell, A. R., Wood, D. M. and Kikumoto, M. (2009). Crushing of particles in idealised granular assemblies. *Journal of the Mechanics and Physics of Solids* 57(8): 1293-1313.

Sadeghi, J. and M. H. Esmaeili (2017). Safe distance of cultural and historical buildings from subway lines. *Soil Dynamics and Earthquake Engineering.* 96: 89-103.

Sadeghi, J., Liravi, H. and Esmaeili, M.H., (2017). Experimental investigation on loading pattern of railway concrete slabs. *Construction and Building Materials*, 153, pp.481-495.

Sadeghi, J. and Esmaeili, M.H., (2018). Effectiveness of track stiffness reduction in attenuation of metro induced vibrations received by historical buildings. *Latin American Journal of Solids and Structures,* 15(11), pp:1-11

Sadeghi, J., Esmaeili, M.H. and Akbari, M., (2019). Reliability of FTA general vibration assessment model in prediction of subway induced ground borne vibrations. *Soil dynamics and earthquake engineering*, *117*, pp.300-311.

Selig, E. T. and Waters, J. M. (1994). Track geotechnology and substructure management, Thomas Telford, London.

Senetakis, K., Anastasiadis, A. and Pitilakis, K. (2012). Dynamic properties of dry sand/rubber (SRM) and gravel/rubber (GRM) mixtures in a wide range of shearing strain amplitudes. Soil Dynamics and Earthquake Engineering, 33(1), pp.38-53.

Shan, Y., S. Zhou, B. Wang and C. L. Ho (2020). Differential Settlement Prediction of Ballasted Tracks in Bridge-Embankment Transition Zones. *Journal of Geotechnical and Geoenvironmental Engineering*. 146(9): 04020075.

Shukla, S. K. and Yin, J. H. (2006). Fundamentals of Geosynthetic Engineering, Taylor & Francis Group, London, UK.

Soga, K. and O'Sullivan, C. (2010). Modeling of geomaterials behavior. *Soils and Foundations* 50(6): 861-875.

Sol-Sánchez, M., F. Moreno-Navarro and M. C. Rubio-Gámez (2014). The Use of Deconstructed Tires as Elastic Elements in Railway Tracks. *Materials*. 7(8): 5903-5919.

Sol-Sánchez, M., F. Moreno-Navarro and M. C. Rubio-Gámez (2014). The Use of Deconstructed Tires as Elastic Elements in Railway Tracks. *Materials*. 7(8): 5903-5919.Sol-Sánchez, M., Moreno-Navarro, F., Tauste-Martínez, R., Saiz, L. and Rubio-Gámez, M. C. (2020). Recycling Tire-Derived Aggregate as elastic particles under railway sleepers: Impact on track lateral resistance and durability. *Journal of Cleaner Production* 277: 123322.

Song, W., Huang, B., Shu, X., Stránský, J. and Wu, H. (2019). Interaction between Railroad Ballast and Sleeper: A DEM-FEM Approach. *International Journal of Geomechanics* 19(5): 04019030.

Suhr, B., W. A. Skipper, R. Lewis and K. Six (2022). DEM modelling of railway ballast using the Conical Damage Model: a comprehensive parametrisation strategy. *Granular Matter*. 24(1): 40.

Suiker, A. S. J. and Borst, R. (2003). A numerical model for the cyclic deterioration of railway tracks. *International Journal for Numerical methods in Engineering* 57(2003): 441–470.

Sun, Q., Indraratna, B. and Ngo, N. T. (2019). Effect of increase in load and frequency on the resilience of railway ballast. *Géotechnique* 69(9): 833-840.

Todisco, M., Coop, M. and Guo, Q. (2015). The effect of the coordination number on particle crushing. 3rd International Symposium on Geomechanics from Micro to Macro, CRC PRESS-TAYLOR & FRANCIS GROUP.

Tutumluer, E., Huang, H. and Bian, X. (2012). Geogrid-aggregate interlock mechanism investigated through aggregate imaging-based discrete element modeling approach. *International Journal of Geomechanics* 12(4): 391-398.

Tutumluer, E., Qian, Y., Hashash, Y. M. A., Ghaboussi, J. and Davis, D. D. (2013). Discrete element modelling of ballasted track deformation behaviour. *International Journal of Rail Transportation* 1(1-2): 57-73.

Wong, C. P. Y. and Coop, M. R. (2020). Development of inter-particle friction in a railway ballast. *Géotechnique Letters* 10(4): 535-541.

Wu, M., Zhou, F. and Wang, J. (2023). DEM modeling of mini-triaxial test on soil-rock mixture considering particle shape effect. *Computers and Geotechnics* 153: 105110.

Xin, T., Ding, Y., Wang, P. and Gao, L. (2020). Application of rubber mats in transition zone between two different slab tracks in high-speed railway. *Construction and Building Materials* 243: 118219.

Zhao, B., Wang, J., Coop, M. R., Viggiani, G. and JIANG, M. (2015). An investigation of single sand particle fracture using X-ray micro-tomography. *Géotechnique* 65(8): 625-641.

Table 1. Mechanical properties of REAL

Material properties	Values
Thickness, t (mm)	10
Area weight, kg/m^2	8.23
Permeability coefficient, k (cm/sec)	2.5×10^{-4}
Static bedding modulus, C_{stat} (N/mm^3)	0.142[a]
Dynamic bedding modulus, C_{dyn} (N/mm^3), f=5–30 Hz	0.107-0.148[a]

[a]DIN (German Institute for Standardization). (2010). "Mechanical vibration—Resilient elements used in railway tracks. Part V: Laboratory test procedures for under-ballast mats." *45673–5*, Berlin.

Table 2. Micromechanical parameters adopted for DEM simulation of ballast

Parameters	Ballast
Particle density (kg/m^3)	2500
Inter-particle coefficient of friction, μ	0.85
Contact normal stiffness, k_n (N/m)	0.52×10^8
Contact shear stiffness, k_s (N/m)	0.26×10^8
Contact normal stiffness of wall, $k_{n\text{-}wall}$ (N/m)	1.25×10^8
Shear stiffness of wall, $k_{s\text{-}wall}$ (N/m)	0.625×10^8
Damping coefficient, ζ	0.7
Parallel bond normal and shear stiffness, k_p (kPa/m)	4.84×10^8
Parallel bond normal and shear strength, s_p (kPa)	842×10^3
Parallel bond radius multiplier, r_p	0.50

Table 3. Input parameters adopted to simulate capping, subgrade and recycled rubber mat

Capping (sub-ballast)

Density (kg/m^3)	Poisson's ratio, ν	Elastic modulus (MPa)	Cohesion (kPa)	Angle of dilation, ψ (degree)	Friction angle, ϕ (degree)
1,955	0.3	120	2	9.0	39

Subgrade

Density (kg/m^3)	Poisson's ratio, ν	Elastic modulus (MPa)	Cohesion yield stress (kPa)	Angle of dilation, ψ (degree)	Friction angle, ϕ (degree)
1,850	0.3	55	30	9.0	25

Recycled rubber mat (REAL)

Density (kg/m^3)	Poisson's ratio, v	Elastic modulus, E_{rubber_mat} (MPa)	Damping ratio
950	0.44	15.68	0.114

Rubber membrane

Density (kg/m^3)	Poisson's Ratio, ν	Elastic modulus, E_{membr} (MPa)
1060	0.42	34.65

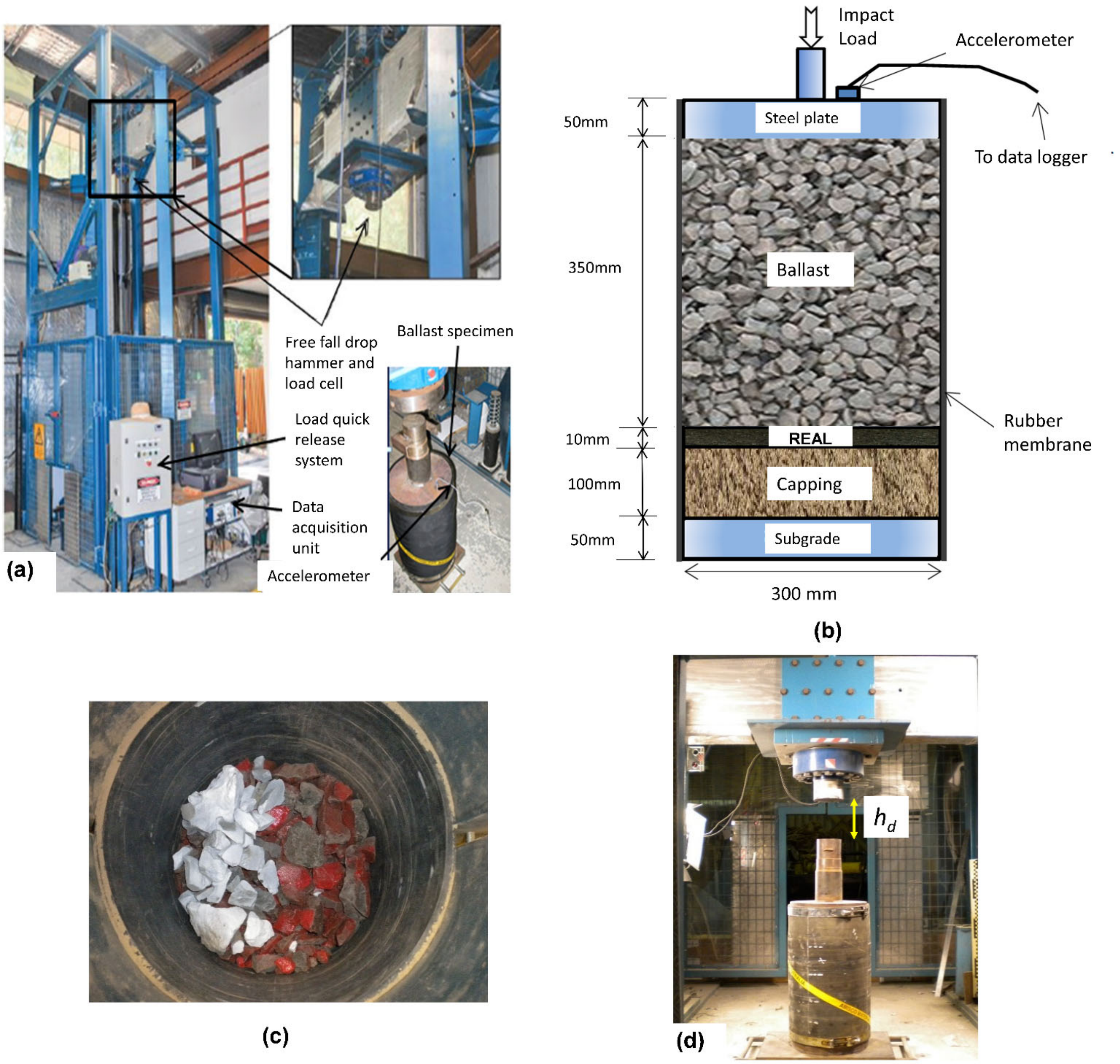

Fig. 1. High capacity impact testing facility: (a) 3D of the impact equipment; (b) schematic diagram of a ballast assembly; (c) placement of ballast into the test specimen; and (d) a ballast sample before the test.

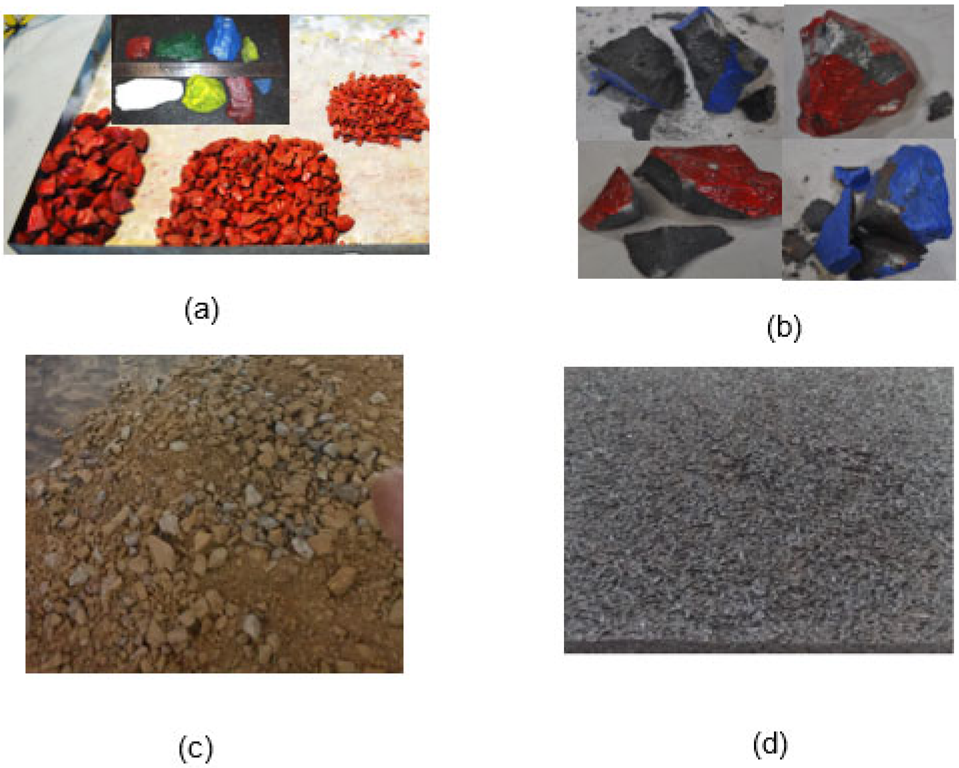

Fig. 2. Typical photos of tested materials: (a) painted clean ballast before the test; (b) ballast breakages after impact tests; (c) capping material and (d) recycled rubber mat (REAL)

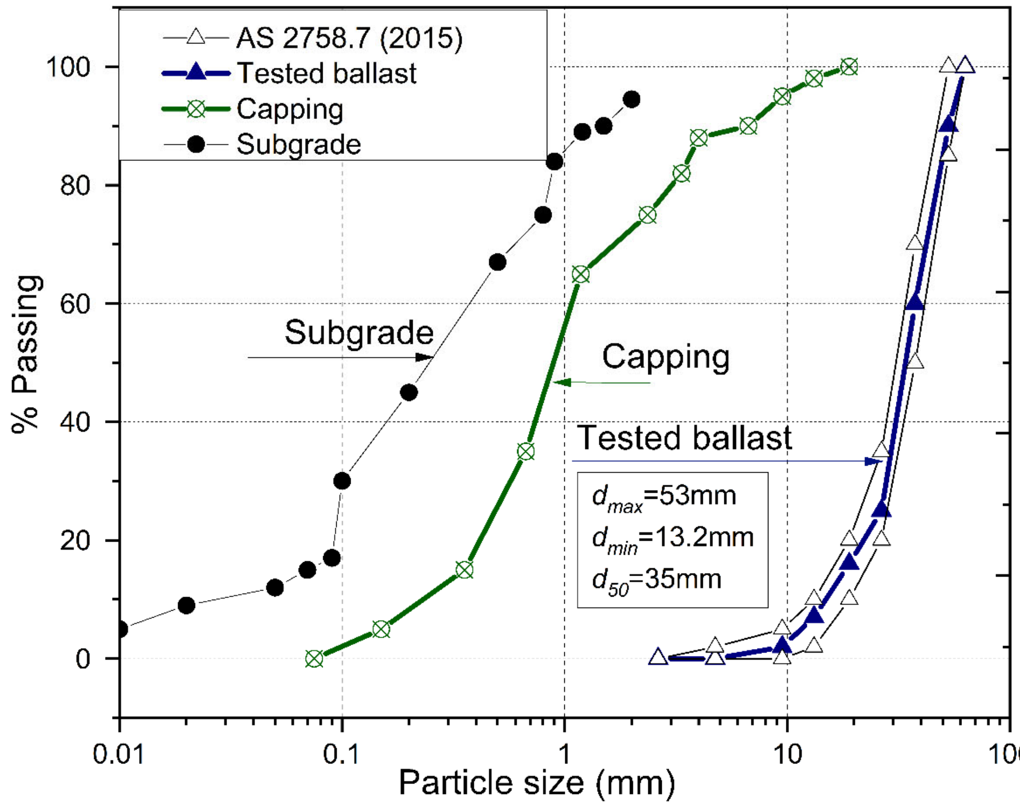

Fig. 3. Particle size distribution of materials used in the laboratory impact tests

(a) (b)

Fig. 4: (a) Actual ballast aggregates used to scan for constructing particles in DEM; (b) Compression test carried out on single ballast

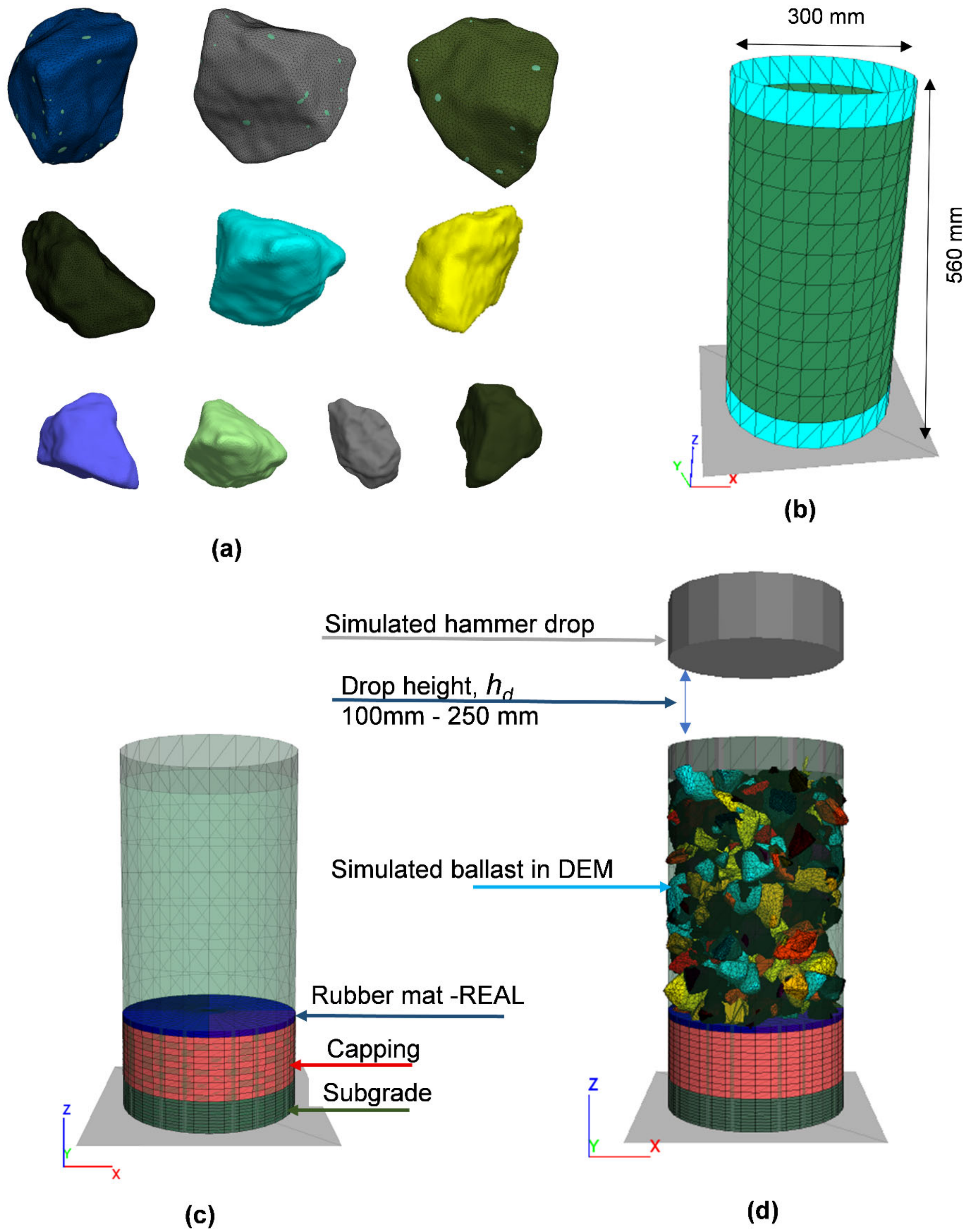

Fig. 5. (a) irregularly-shaped ballast grains simulated in DEM; (b) surrounding rubber membrane; (c) simulated subgrade, capping and REAL; (d) a ballast assembly simulated in DEM before the impact test

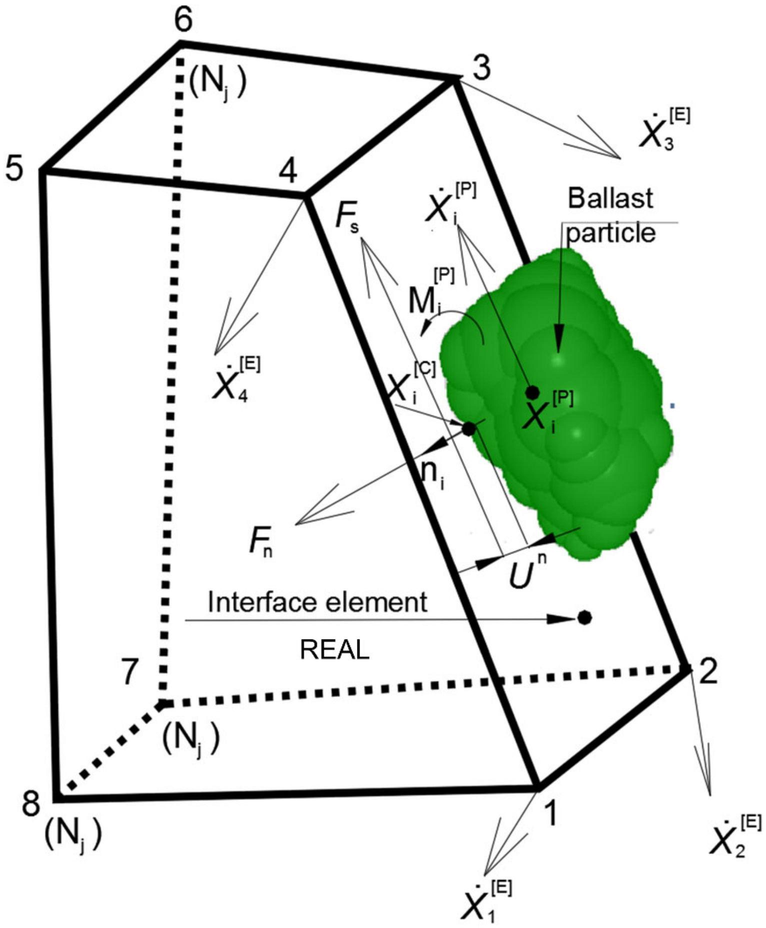

Fig. 6. Schematic diagram of an interface contact between a ballast particle and continuum element

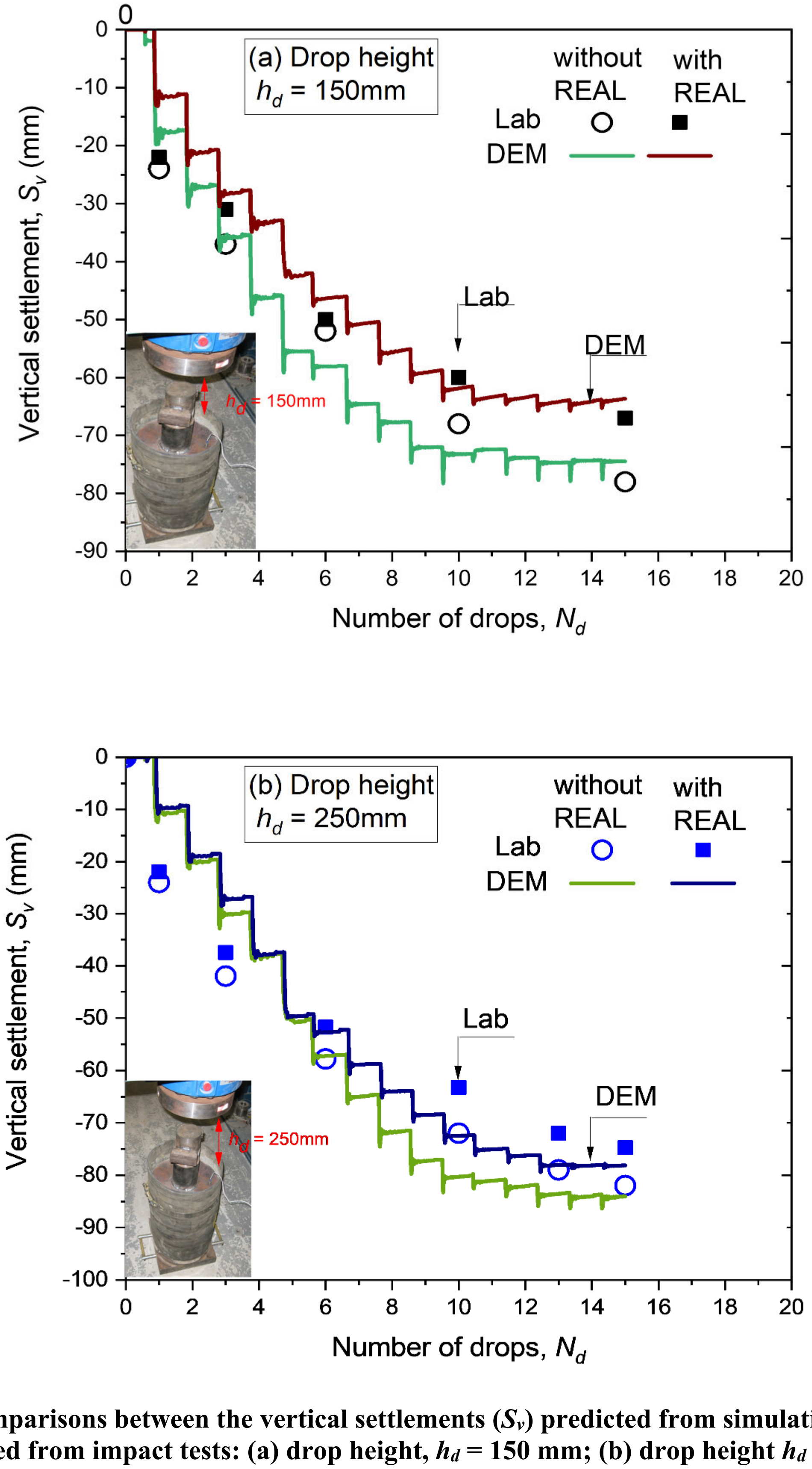

Fig. 7: Comparisons between the vertical settlements (S_v) predicted from simulations with those measured from impact tests: (a) drop height, h_d = 150 mm; (b) drop height h_d = 250 (mm)

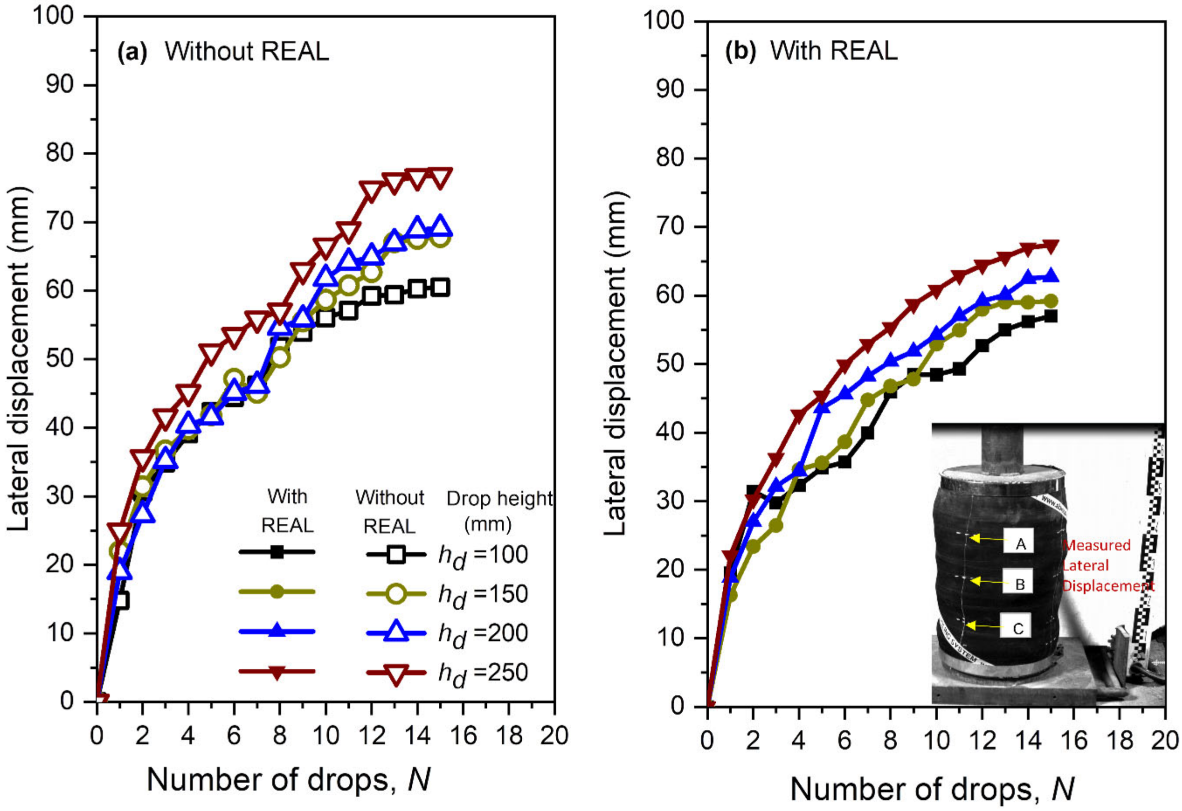

Fig. 8: Measured lateral displacements of ballast assemblies in the laboratory: (a) without REAL; and (b) with REAL

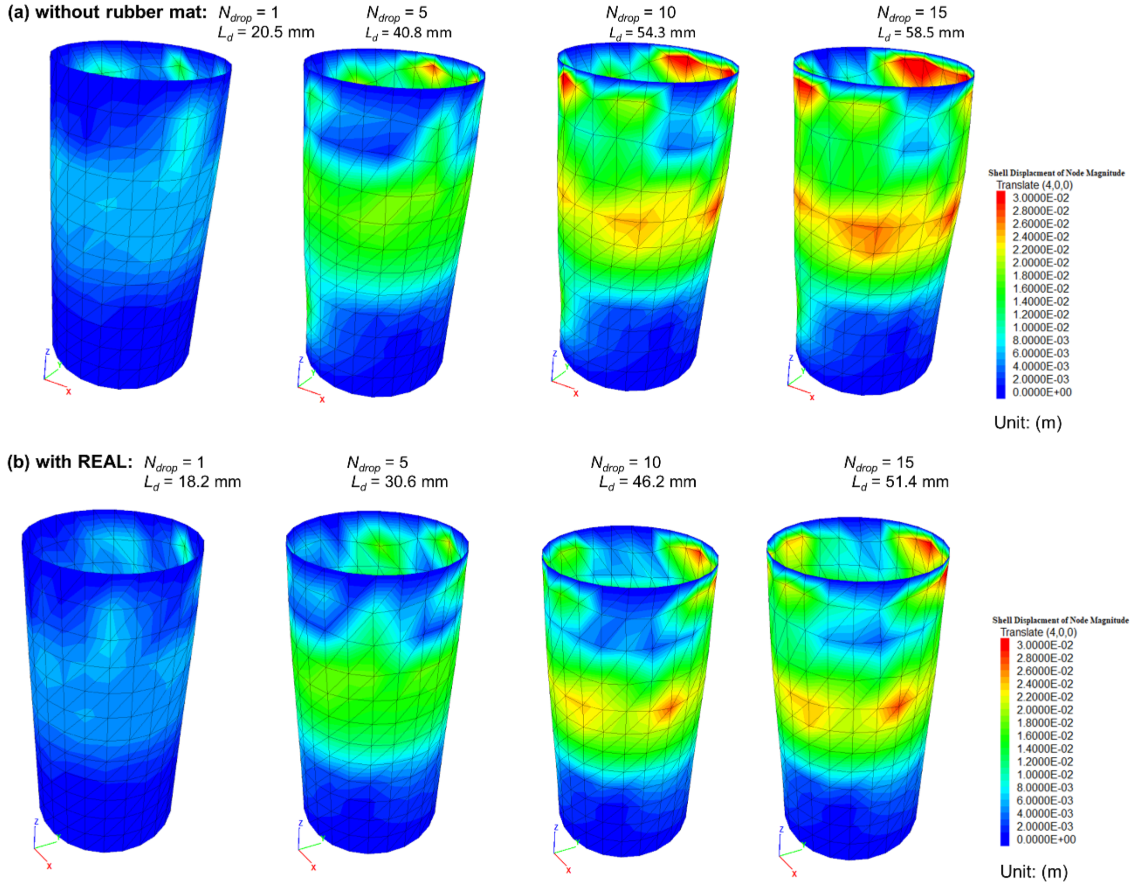

Fig. 9: Predicted lateral displacement of ballast assembly during impact loading tests (drop height, h_d = 150mm): (a) without recycled rubber mat, REAL; (b) with REAL

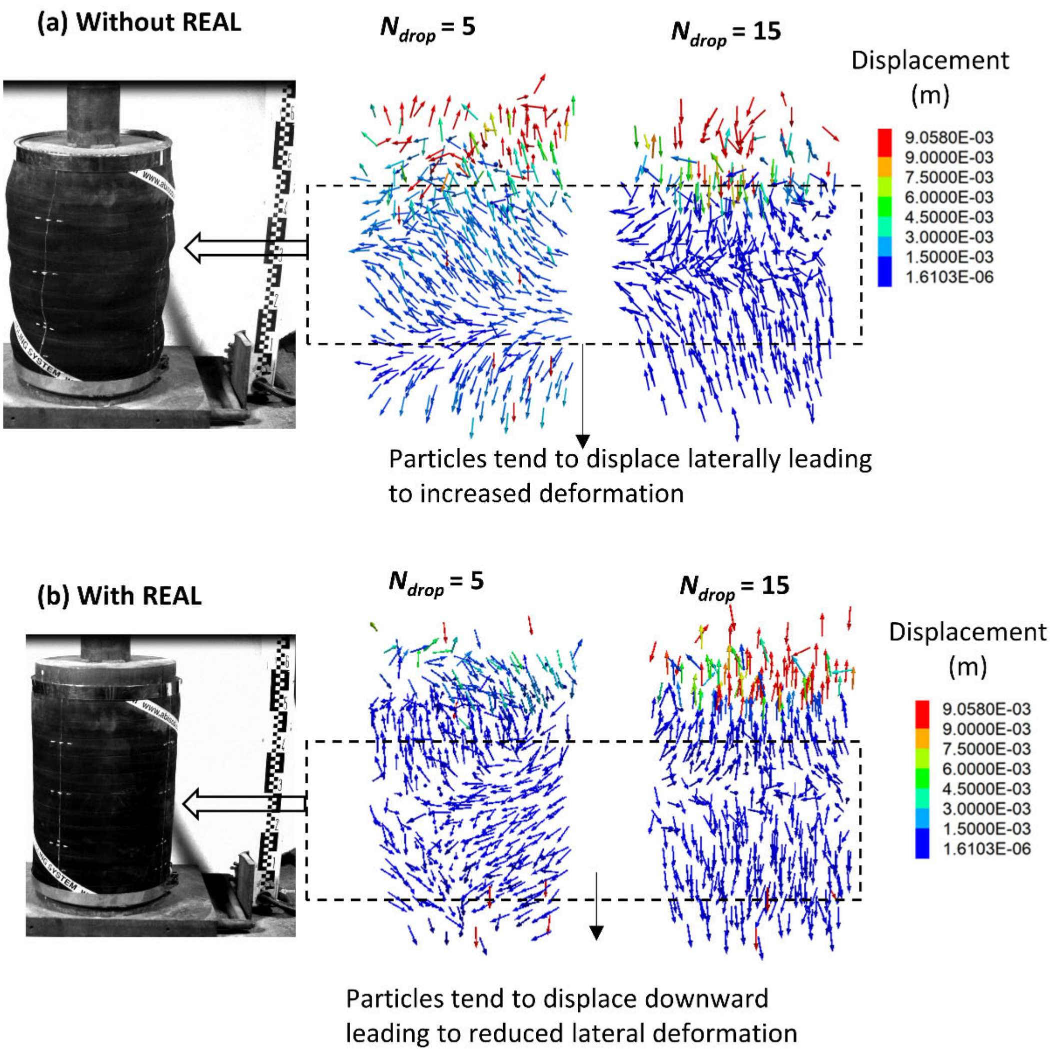

Fig. 10. Displacement vectors of ballast: (a) without REAL; and (b) with REAL

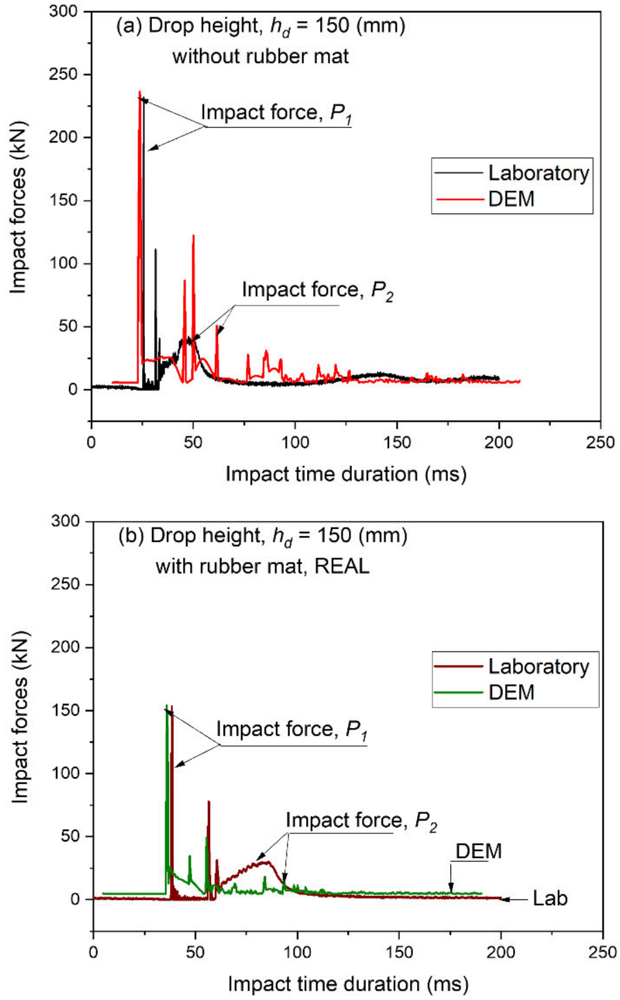

Fig. 11. Comparison of predicted impact forces with those measure in laboratory: (a) without REAL; and (b) with REAL

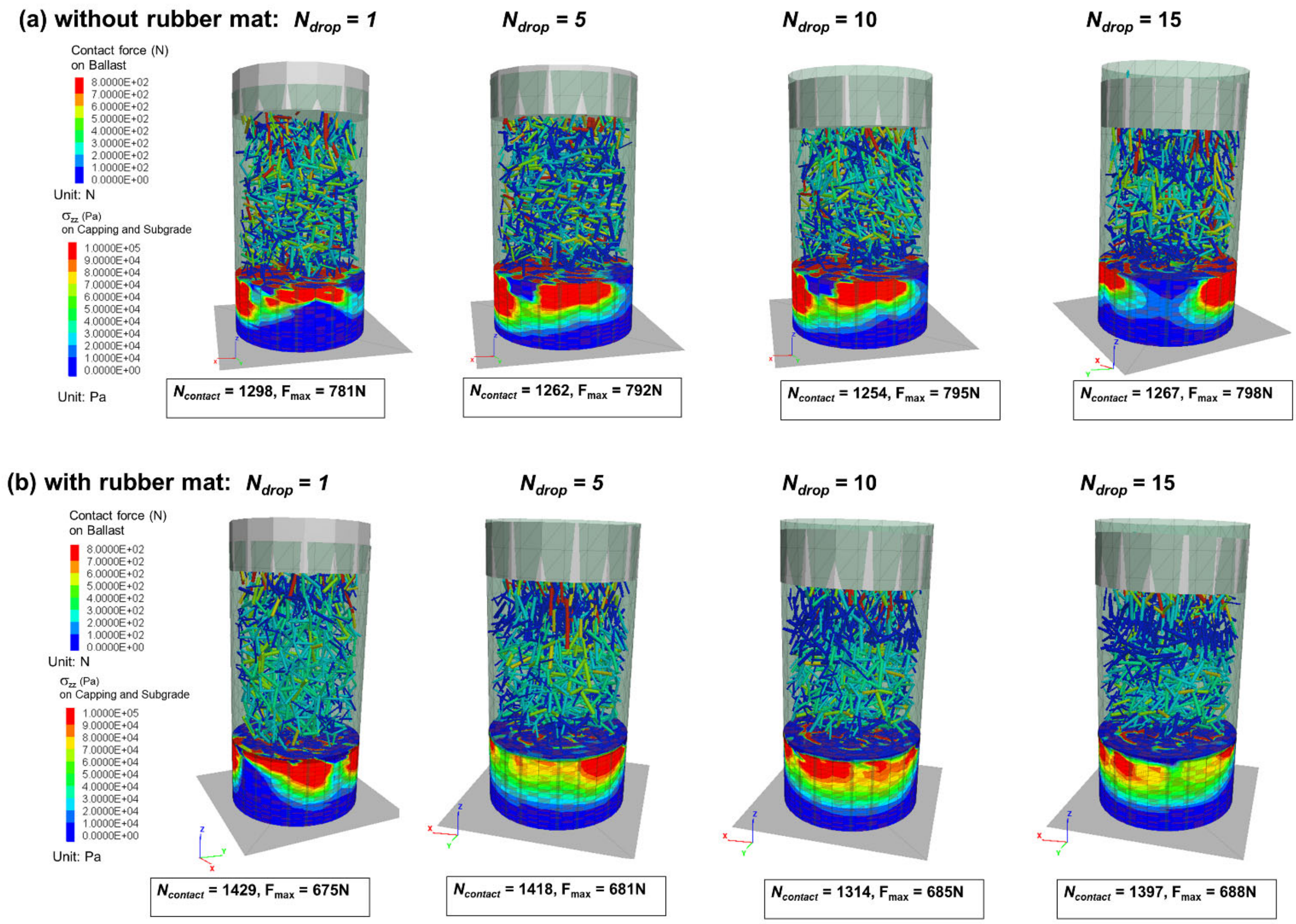

Fig. 12. Predicted contact force distribution captured at different numbers of hammer drops: (a) without the inclusion of REAL; and (b) with REAL

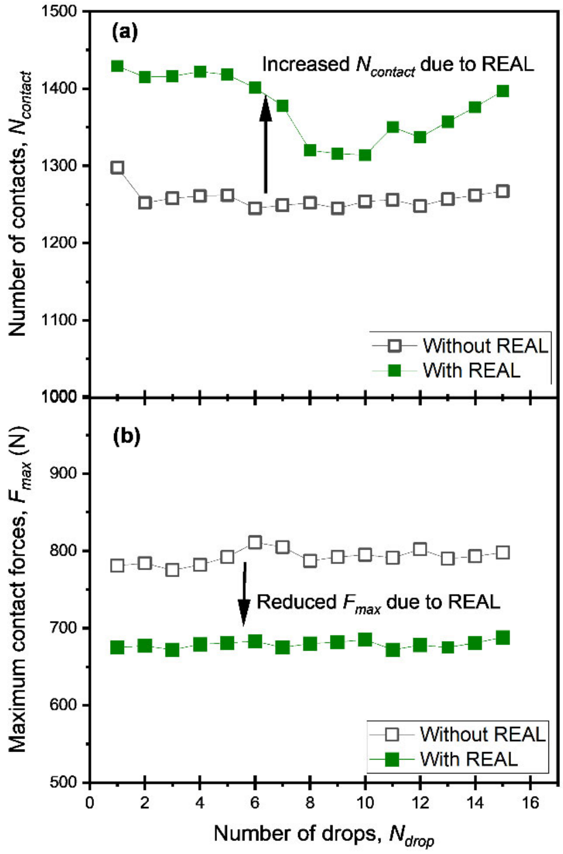

Fig. 13. (a) Evolution of number of contacts; (b) changes of maximum contact forces of ballast with and without the inclusion of REAL

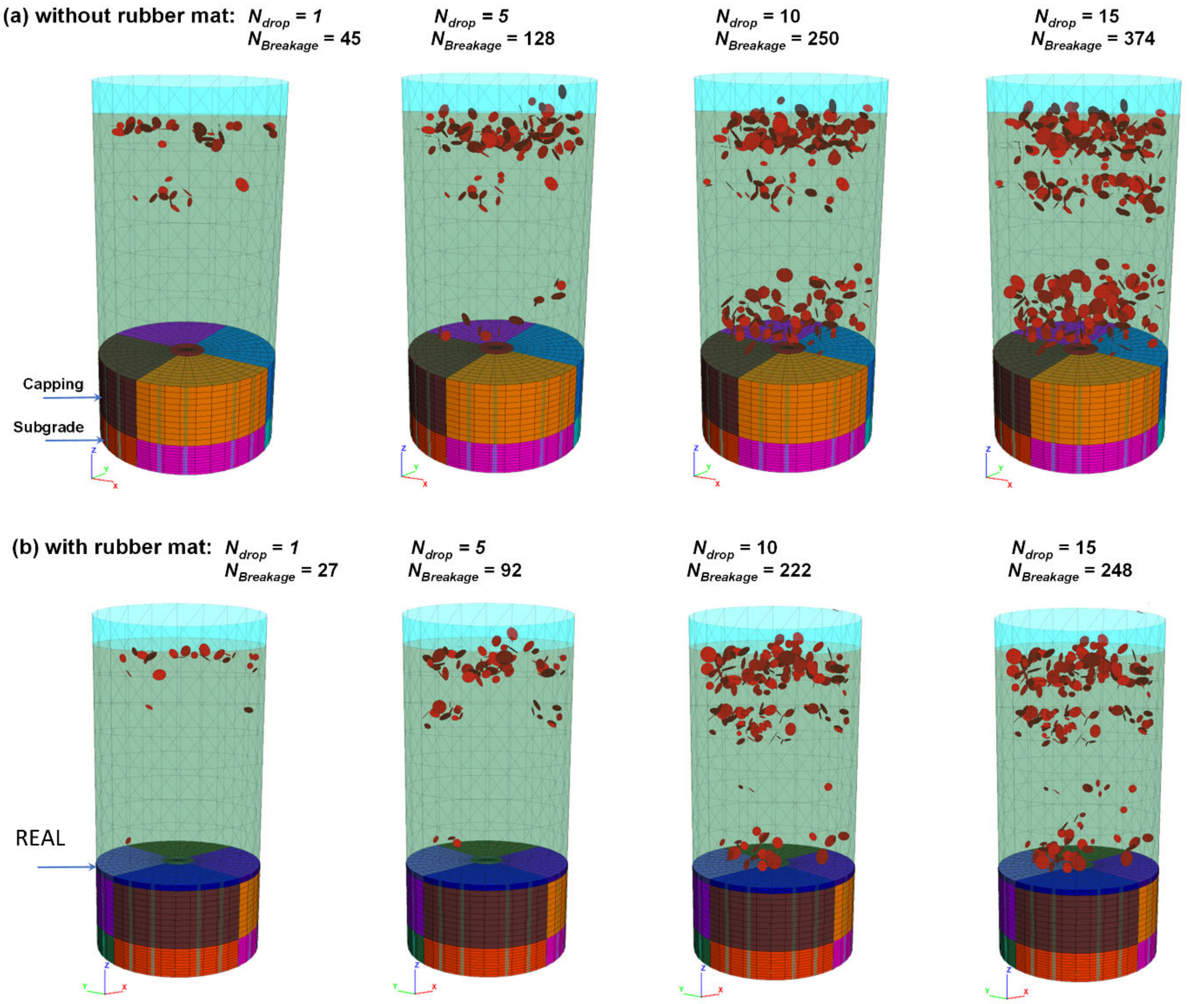

Fig. 14. Evolution of broken bonds ($N_{Breakage}$) captured at different numbers of hammer drop, N_{drop}, subjected to a drop height of h_d = 200 mm: (a) without REAL; and (b) with REAL

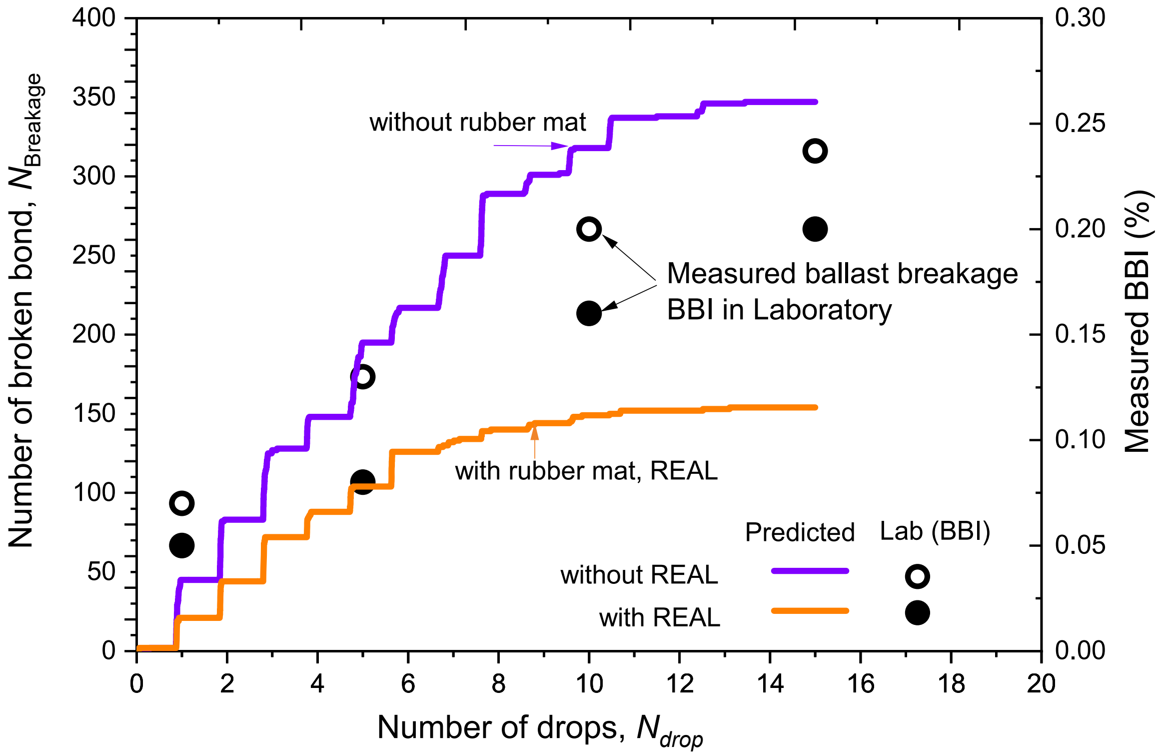

Fig. 15. Evolution of simulated number of broken bond ($N_{beakage}$) and measured ballast breakage index (BBI) with number of hammer drops for a given drop height of h_d = 150mm

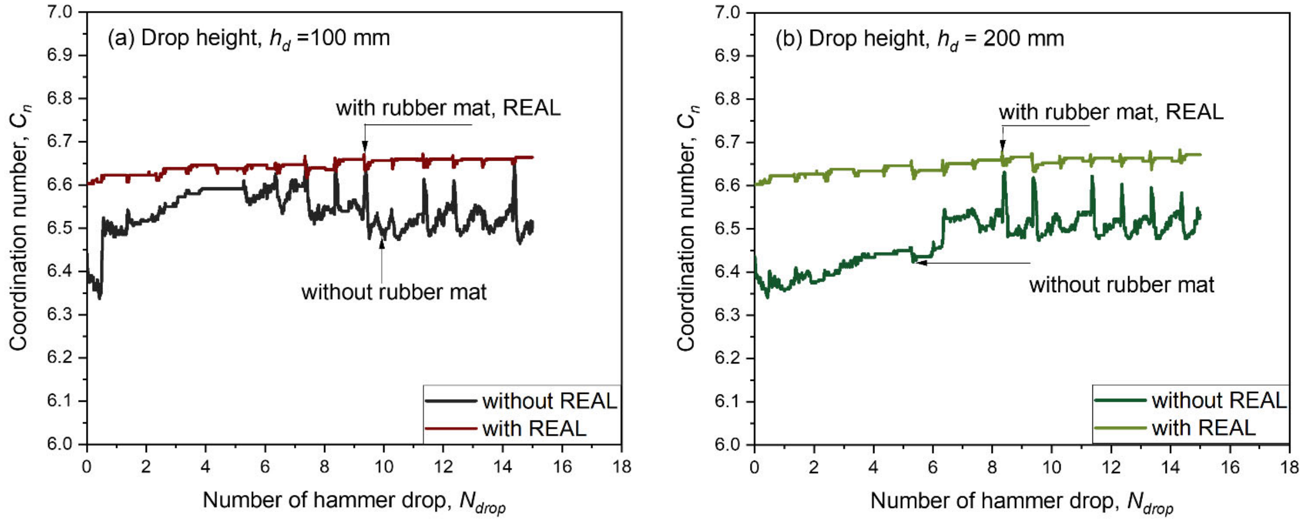

Fig. 16. Evolutions of coordination number, C_n with increased hammer drops: (a) drop height, h_d=100 mm; (b) drop height, h_d=200 mm

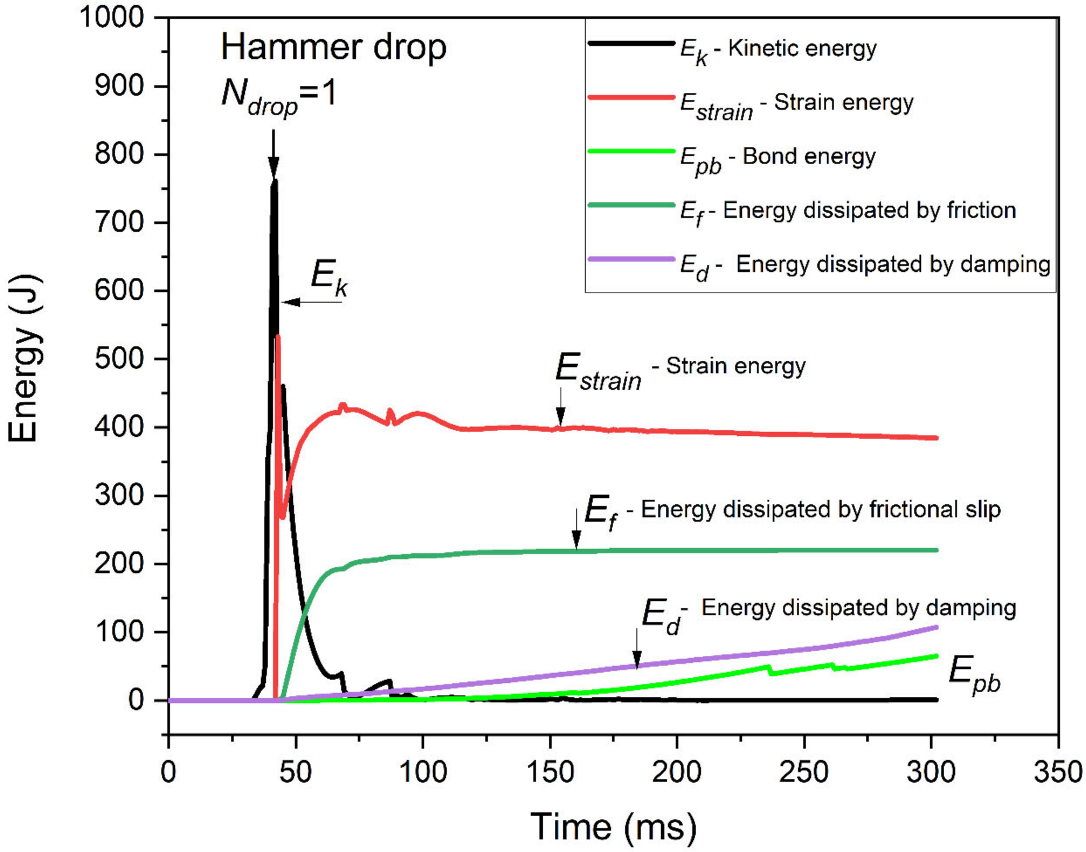

Fig. 17. Predicted energy components during an impact test captured at N_{drop}=1 of a ballast assembly with the inclusion of REAL under a drop height of h_d =100mm

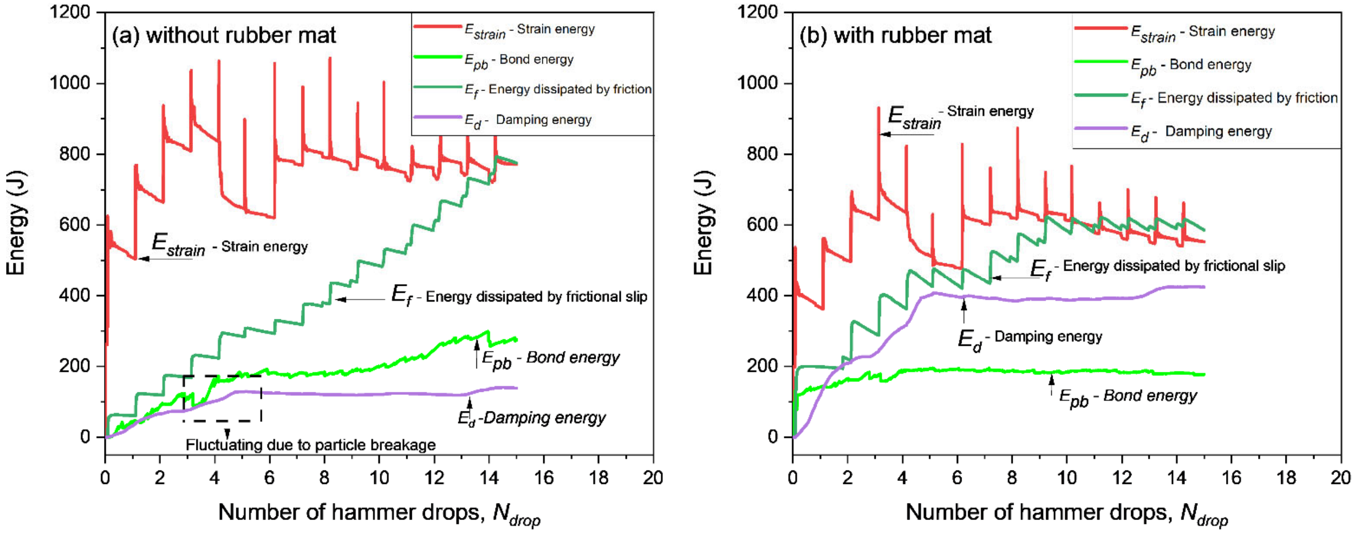

Fig. 18. Evolution of energy components versus number of hammer drop (N_{drop}): (a) without inclusion of rubber mat; and (b) with inclusion of rubber mat, REAL

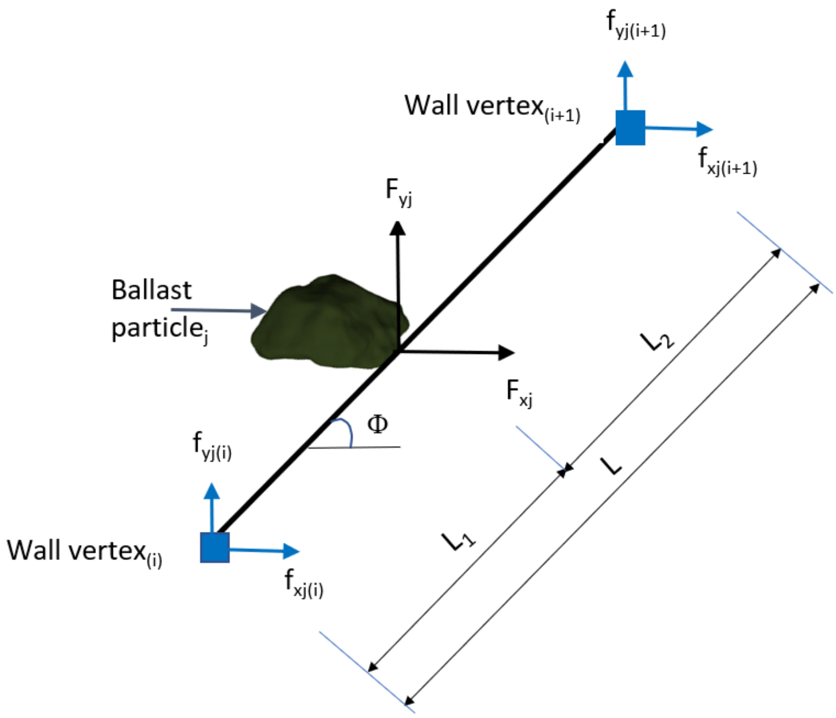

Fig. 19. Schematic diagram for transferring contact forces to nodal forces

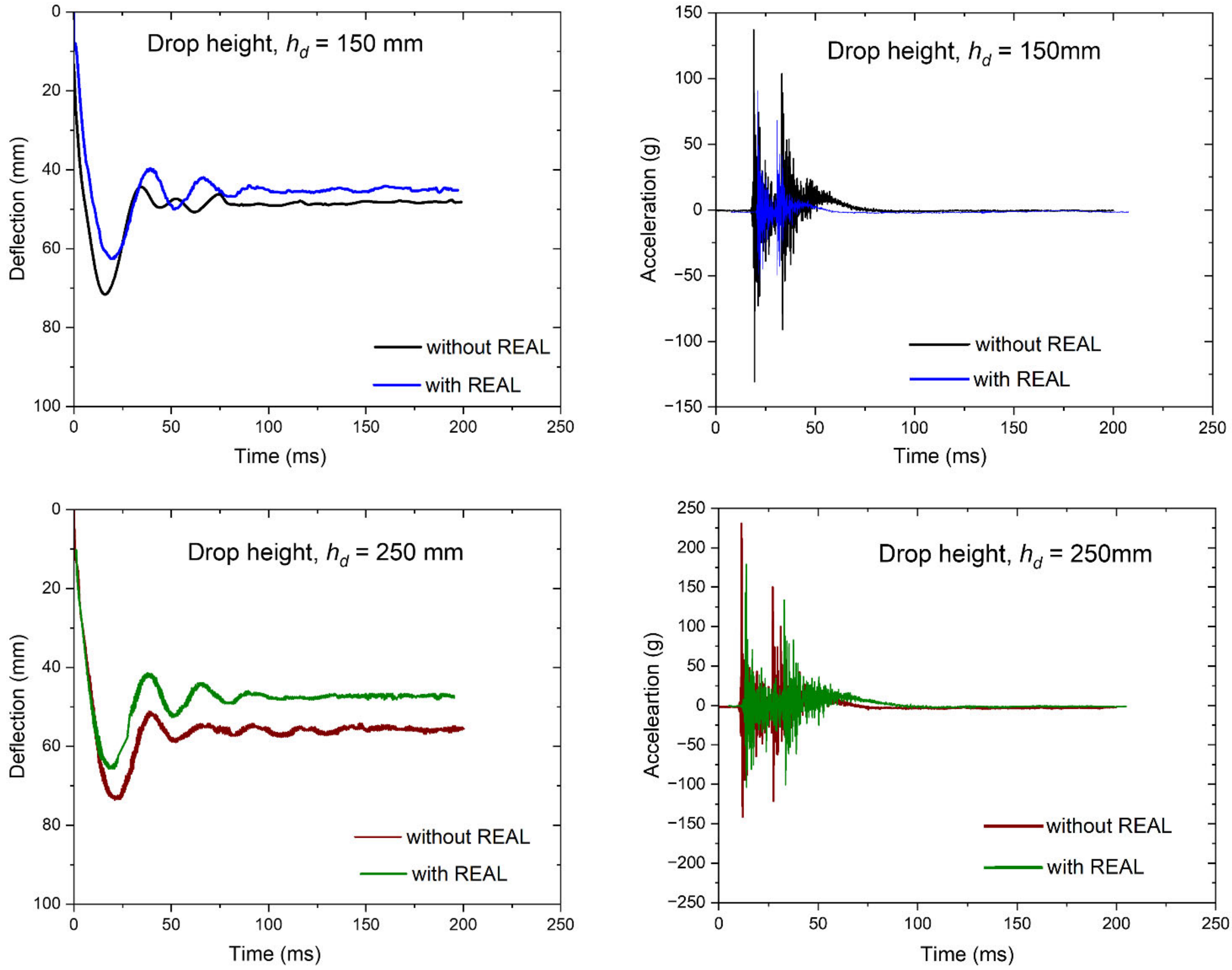

Fig. 20: Output signals of deflection and acceleration recorded from impact tests under drop heights, h_d = 150, 250 mm at N_{drop}=5